

# Magnetic fields in barred galaxies

## I. The atlas

R. Beck<sup>1</sup>, V. Shoutenkov<sup>2</sup>, M. Ehle<sup>3,4</sup>, J. I. Harnett<sup>5</sup>, R. F. Haynes<sup>6</sup>, A. Shukurov<sup>7</sup>, D. D. Sokoloff<sup>8</sup>,  
M. Thierbach<sup>1</sup>

<sup>1</sup> Max-Planck-Institut für Radioastronomie, Auf dem Hügel 69, D-53121 Bonn, Germany

<sup>2</sup> Pushchino Radioastronomy Observatory, Astro Space Center, 142292 Pushchino, Russia, & Isaac Newton Institute of Chile, Pushchino Branch

<sup>3</sup> XMM-Newton Science Operations Centre, Apdo. 50727, 28080 Madrid, Spain

<sup>4</sup> Research and Scientific Support Department of ESA, ESTEC, Postbus 299, 2200 AG Noordwijk, The Netherlands

<sup>5</sup> University of Technology Sydney, P.O. Box 123, Broadway 2007, NSW, Australia

<sup>6</sup> School of Mathematics and Physics, University of Tasmania, GPO Box 252-21, Hobart, Tas 7001, Australia

<sup>7</sup> Department of Mathematics, University of Newcastle, Newcastle upon Tyne NE1 7RU, UK

<sup>8</sup> Department of Physics, Moscow University, 119899 Moscow, Russia

Received 13 Feb 2002 / Accepted 29 April 2002

**Abstract.** The total and polarized radio continuum emission of 20 barred galaxies was observed with the Very Large Array (VLA) at  $\lambda$ 3, 6, 18 and 22 cm and with the Australia Telescope Compact Array (ATCA) at  $\lambda$ 6 cm and 13 cm. Maps at 30'' angular resolution are presented here. Polarized emission (and therefore a large-scale regular magnetic field) was detected in 17 galaxies. Most galaxies of our sample are similar to non-barred galaxies with respect to the radio/far-infrared flux correlation and equipartition strength of the total magnetic field. Galaxies with highly elongated bars are not always radio-bright. We discuss the correlation of radio properties with the aspect ratio of the bar and other measures of the bar strength. We introduce a new measure of the bar strength,  $\Lambda$ , related to the quadrupole moment of the bar's gravitational potential. The radio surface brightness  $I$  of the barred galaxies in our sample is correlated with  $\Lambda$ ,  $I \propto \Lambda^{0.4 \pm 0.1}$ , and thus is highest in galaxies with a long bar where the velocity field is distorted by the bar over a large fraction of the disc. In these galaxies, the pattern of the regular field is significantly different from that in non-barred galaxies. In particular, field enhancements occur upstream of the dust lanes where the field lines are oriented at large angles to the bar's major axis. Polarized radio emission seems to be a good indicator of large-scale non-axisymmetric motions.

**Key words.** Galaxies: magnetic fields – Galaxies: individual: NGC986, NGC1097, NGC1300, NGC1313, NGC1365, NGC1433, NGC1493, NGC1559, NGC1672, NGC2336, NGC2442, NGC3059, NGC3359, NGC3953, NGC3992, NGC4535, NGC5068, NGC5643, NGC7479, NGC7552 – Galaxies: spiral – Galaxies: structure – ISM: magnetic fields

## 1. Introduction

Polarization observations in radio continuum have revealed basic properties of interstellar magnetic fields in a few dozen spiral galaxies (Beck et al. 1996, Beck 2000). Large-scale regular fields form spiral patterns with pitch angles similar to those of the optical spiral arms. The strongest *regular* fields usually occur between the optical arms, sometimes concentrated in 'magnetic arms' (Beck & Hoernes 1996). The *total* (= polarized + unpolarized) nonthermal (synchrotron) radio emission is a tracer of the *total* field which comprises both regular and random field

components. It generally peaks on the optical arms because the random field is strongest there. This distinction implies that the regular and random magnetic fields are maintained and affected by different physical processes.

Spiral patterns of the regular magnetic field are believed to be generated by dynamo action in a differentially rotating disc (Beck et al. 1996). The dynamo reacts or interacts with non-axisymmetric disturbances like density waves (Mestel & Subramanian 1991, Rohde et al. 1999), but little is known about the effects of bar-like distortions. Chiba & Lesch (1994) suggested that a bar may excite higher dynamo modes, while Moss et al. (1998) found

from their models a mixture of modes with rapidly changing appearance.

Radio observations of barred galaxies are rare. The angular resolution of the maps in Condon’s (1987) atlas was insufficient to distinguish emission from the bar, the spiral arms and the halo. Another survey of barred galaxies in radio continuum by García-Barreto et al. (1993) had even lower angular resolution; neither survey included polarization. The first high-resolution radio map of a barred galaxy, NGC 1097 (Ondrechen & van der Hulst 1983), showed narrow ridges in total intensity coinciding with the dust lanes, which are tracers of compression regions along the leading (with respect to the sense of rotation) edge of the bar. A similar result was obtained for M83 (Ondrechen 1985) which hosts a bar of smaller size than NGC 1097. No polarization could be detected in NGC 1097 by Ondrechen & van der Hulst (1983). Radio observations of NGC 1365 at  $\lambda\lambda 20$ , 6 and 2 cm, restricted to a central region, have revealed similar features (Jörsäter & van Moorsel 1995). The first detection of polarized radio emission from the bar region was reported by Ondrechen (1985) for M83, with a mean fractional polarization at  $\lambda 6$  cm of 25%. Neininger et al. (1991) mapped the polarized emission from M83 at  $\lambda 2.8$  cm. They showed that the regular magnetic field in the bar region is aligned with the bar’s major axis. Observed with higher resolution, the regular field is strongest at the leading edges of the bar of M83 (Beck 2000).

Another barred galaxy which has been studied in detail in radio polarization is NGC 3627 (Soida et al. 2001). The regular field in the bar region is again aligned parallel to the bar’s major axis, being strongest at the leading edges of the bar. However, east of the bar the field behaves anomalously, forming a ‘magnetic arm’ crossing the gaseous arm.

The first high-resolution polarization observations of a galaxy with a massive bar, NGC 1097, were presented by Beck et al. (1999). The magnetic field lines in and around the bar appear to follow the velocity field of the gas expected from a generic gas dynamic model (Athanasoula 1992). The regular magnetic field outside the bar region has a spiral pattern similar to that seen optically. A narrow ridge of greatly reduced polarized intensity indicates the deflection of the field lines in a shear shock (the dust lane), but the magnetic field lines turn more smoothly than the gas streamlines (Moss et al. 2001, hereafter Paper II). Velocity fields are available from HI observations only for the outer parts of NGC 1097 (Ondrechen et al. 1989) and from CO observations only for the circumnuclear ring (Gerin et al. 1988).

NGC 1097 is one of the objects in our sample of barred galaxies observed with the VLA and the ATCA. In this paper we present the full set of radio maps of our survey, smoothed to a common resolution of  $30''$ , and give an overview of their salient properties. Higher-resolution maps of NGC 1097, 1365 and 7479 will be presented and discussed in subsequent papers. New dynamo models for barred galaxies are discussed in Paper II. Further details

on the magnetic fields in NGC1672, 2442 and 7552 will be given by Harnett et al. (2002, hereafter Paper III).

## 2. The sample

Table 1 lists the barred galaxies that have been observed with the VLA (declinations north of  $-39^\circ$ ). These have an optical extent  $\geq 4'$ , to obtain reasonable spatial resolution, a mean total intensity in radio continuum of  $\geq 3$  mJy/arcmin<sup>2</sup>, and were selected from Condon’s (1987) survey. Our sample of galaxies observed with the ATCA (declinations south of  $-39^\circ$ ) is shown in Table 2. The criteria are the same, except for the size limit of  $3'$ . The isophotal major-axis diameter in arcmin is denoted by  $d_{25}$ , and  $q_{25}$  is the ratio of the major-to-minor isophotal diameters; the subscript 25 refers to the isophotal level of 25 mag/arcsec<sup>2</sup>. The systemic velocity  $v_{\text{GSR}}$  has been transformed into distance  $D$  using  $H_0=75$  km s<sup>-1</sup> Mpc<sup>-1</sup>, except for NGC 1365 and NGC 4535, for which Cepheid distances are available (Madore et al. 1998, Macri et al. 1999). The inclination and position angle of each projected galaxy disc are denoted  $i$  and PA (Martin 1995; Martin & Friedli 1997; Ma et al. 1997, 1998; Wilke et al. 2000; Möllenhoff & Heidt 2001);  $i = 0$  means face-on and PA = 0 is the north-south direction. For several southern galaxies, no values of  $i$  and PA are available, as indicated by ‘?’. The deprojected ratio of the bar’s minor and major axes is denoted  $b/a$ , and  $2a/d_{25}$  is its relative length according to Elmegreen & Elmegreen (1985) or Martin (1995), derived from deprojected images according to the galaxy’s inclination and position angle, assuming that the bars are flat. Values in brackets are our estimates from optical images.

The far-infrared flux densities at  $\lambda 60 \mu\text{m}$ , denoted  $S_{60\mu\text{m}}$ , are from Fullmer & Lonsdale (1989). Their values for NGC 2442 and NGC 3992 are obviously underestimated and were recalculated from the flux density at  $100 \mu\text{m}$  using  $S_{60\mu\text{m}} = f S_{100\mu\text{m}}$  with  $f = 0.5$  for the luminous galaxy NGC 2442 and  $f = 0.3$  for the faint galaxy NGC 3992 (see Fig. 5b in Young et al. 1989). The integrated radio continuum flux densities at  $\lambda 20$  cm and  $\lambda 6$  cm,  $S_{20\text{cm}}^{\text{tot}}$  in Table 1 and  $S_{6\text{cm}}^{\text{tot}}$  in Table 2, were taken from Condon (1987) and Whiteoak (1970), respectively.

## 3. Observations and results

The observations were performed with the VLA operated by the NRAO<sup>1</sup> and with the ATCA<sup>2</sup> operated by the ATNF. Details of the observations are given in Tables 3 and 4. The antenna configurations were chosen to obtain half-power widths of the synthesized beams of about  $20''$ .

<sup>1</sup> The National Radio Astronomy Observatory is a facility of the National Science Foundation operated under cooperative agreement by Associated Universities, Inc.

<sup>2</sup> The Australia Telescope Compact Array is part of the Australia Telescope which is funded by the Commonwealth of Australia for operation as a National Facility managed by CSIRO.

**Table 1.** The VLA sample of barred galaxies

NGC	Hubble type (1)	Lum. class (1)	RC3 class (2)	R.A. (2000) [h m s]	Dec. (2000) [° ' "]	$d_{25}$ [''] (2)	$q_{25}$ (2)	$v_{\text{GSR}}$ [km/s] (2)	$D$ [M pc]	$i$ [°]	PA [°]	$b/a$	$2a/d_{25}$	$S_{60\mu\text{m}}$ [Jy] (3)	$S_{20\text{cm}}^{\text{tot}}$ [mJy] (4)
1097	SBbc(rs)	I-II	SBS3	02 46 19.0	-30 16 21	9.3	1.48	1193	16	45	135	[0.4]	0.37	45.9	415
1300	SBb(s)	I.2	SBT4	03 19 40.9	-19 24 41	6.2	1.51	1496	20	35	86	[0.3]	0.41	2.4	35
1365	SBb(s)	I	SBS3	03 33 36.7	-36 08 17	11.2	1.82	1541	19	40	40	0.51	0.47	78.2	530
2336	SBbc(r)	I	SXR4	07 27 04.4	+80 10 41	7.1	1.82	2345	31	59	178	0.41	0.17	1.0	18
3359	SBc(s)	I.8	SBT5	10 46 37.8	+63 13 22	7.2	1.66	1104	15	55	170	0.32	0.25	4.1	50
3953	SBbc(r)	I-II	SBR4	11 53 49.6	+52 19 39	6.9	2.00	1122	15	61	13	0.89	0.17	2.9	41
3992	SBb(rs)	I	SBT4	11 57 36.3	+53 22 31	7.6	1.62	1121	15	59	67	0.58	0.27	$\approx$ 3	21
4535	SBc(s)	I.3	SXS5	12 34 20.4	+08 11 53	7.1	1.41	1892	16	26	28	[0.6]	[0.1]	6.5	65
5068	SBc(s)	II-III	SXT6	13 18 55.4	-21 02 21	7.2	1.15	550	7	29	110	0.44	0.16	2.3	39
7479	SBbc(s)	I-II	SBS5	23 04 57.2	+12 19 18	4.1	1.32	2544	34	45	25	0.41	0.46	12.1	109

References: (1) Sandage & Tammann (1981); (2) de Vaucouleurs et al. (1991); (3) Fullmer & Lonsdale (1989); (4) Condon (1987).

**Table 2.** The ATCA sample of barred galaxies

NGC	Hubble type (1)	Lum. class (1)	RC3 class (2)	R.A. (2000) [h m s]	Dec. (2000) [° ' "]	$d_{25}$ [''] (2)	$q_{25}$ (2)	$v_{\text{GSR}}$ [km/s] (2)	$D$ [M pc]	$i$ [°]	PA [°]	$b/a$	$2a/d_{25}$	$S_{60\mu\text{m}}$ [Jy] (3)	$S_{6\text{cm}}^{\text{tot}}$ [mJy] (4)
986	SBb(rs)	I-II	SBT2	02 33 34.3	-39 02 43	3.9	1.32	1907	25	?	?	[0.5]	0.46	23.1	40
1313	SBc(s)	III-IV	SBS7	03 18 15.5	-66 29 51	9.1	1.32	292	4	38	170	0.63	0.31	10.4	59
1433	SBb(s)	I-II	PSBR2	03 42 01.4	-47 13 17	6.5	1.10	920	12	27	17	0.33	0.36	3.3	-
1493	SBc(rs)	III	SBR6	03 57 27.9	-46 12 38	3.5	1.07	900	12	30	?	0.32	0.18	2.2	-
1559	SBc(s)	II.8	SBS6	04 17 37.4	-62 47 04	3.5	1.74	1115	15	55	65	[0.3]	[0.2]	23.8	120
1672	SBb(rs)	II	SBS3	04 45 42.2	-59 14 57	6.6	1.20	1155	15	39	170	0.41	0.68	34.8	100
2442	SBbc(rs)	II	SXS4P	07 36 23.9	-69 31 50	5.5	1.12	1236	16	24	40	[0.5]	0.42	$\approx$ 22	70
3059	SBc(s)	III	SBT4	09 50 08.1	-73 55 17	3.6	1.12	1056	14	?	?	[0.3]	[0.2]	9.6	-
5643	SBc(s)	II-III	SXT5	14 32 41.5	-44 10 24	4.6	1.15	1066	14	?	?	[0.4]	[0.35]	18.7	64
7552	SBbc(s)	I-II	PSBS2	23 16 11.0	-42 35 01	3.4	1.26	1568	21	31	1	0.29	0.59	72.9	140

References: (1)–(3) see Table 1; (4) Whiteoak (1970).

In the L band, VLA observations were performed at 1365 MHz ( $\lambda$ 22 cm) and 1665 MHz ( $\lambda$ 18 cm) simultaneously. In each of the VLA C and X bands, the data from two channels were combined (4835 MHz + 4885 MHz and 8435 MHz + 8485 MHz). The four southern galaxies from the VLA sample were observed with hybrid configurations (CnB and DnC) which allow to synthesize a more circular beam. For NGC 1097, the CnB and DnC  $uv$  data at the same wavelength were combined.

Several ATCA 750 m configurations were combined at  $\lambda$ 5.8 cm (4800 MHz + 5568 MHz) to achieve higher sensitivity and better coverage of the  $uv$  plane. For three large galaxies, additional observations with the ATCA 375 m configuration were added. In two observation sessions (1993 May 19 and 1998 January 9), data at 1380 MHz ( $\lambda$ 22 cm) and at 2368 MHz ( $\lambda$ 13 cm) were recorded simultaneously. No significant polarization was detected at  $\lambda$ 22 cm. In the session of 1996 October 29, frequencies were set to 2240 MHz ( $\lambda$ 13.4 cm) and 2368 MHz ( $\lambda$ 12.7 cm). In the sessions of 1993 July 26 and September 9, data at 4800 MHz ( $\lambda$ 6.2 cm) and at 8640 MHz ( $\lambda$ 3.5 cm) were recorded simultaneously.

The largest visible structure for full synthesis observations (that requires an observing time in excess of 8 h with the VLA or 12 h with the ATCA) is  $15'$  at  $\lambda$ 18 cm and 22 cm (VLA C or CnB arrays),  $5'$  at  $\lambda$ 6 cm (VLA D or DnC arrays),  $3'$  at  $\lambda$ 3 cm (VLA D or DnC arrays),  $3'$  at  $\lambda$ 13 cm (ATCA 1.5 km arrays),  $4'$  at  $\lambda$ 6 cm (ATCA 750 m arrays) and  $8'$  at  $\lambda$ 6 cm (ATCA 375 m array).

The data were reduced with the standard AIPS and MIRIAD software packages. The maps in Stokes parameters I, Q and U were smoothed to a common resolution of  $30''$  to achieve a higher signal-to-noise ratio. These were combined to maps of total and polarized surface brightness<sup>3</sup>, measured in Jansky per solid angle of the telescope beam ('beam area'), and polarization angle. The positive bias in PI due to noise was corrected by subtraction of a constant value, which is equal to  $1.0\text{--}1.4 \times (\text{rms noise})$  in the maps of Q and U.

The rms noise in the final maps in I (total intensity) and PI (polarized intensity) is given in Tables 3 and 4. Since the noise in the PI maps has a non-Gaussian distribution (even if Q and U have Gaussian noise) the standard deviation underestimates the noise. Therefore we assume the noise in PI to be the same as that in Q and U. The rms noise in the ATCA maps is typically larger by a factor two in comparison to the VLA maps.

The final maps are displayed in Figs. 5–24, overlaid onto images from the Digitized Sky Surveys.<sup>4</sup> Contours show the total intensity at the wavelength indicated near

<sup>3</sup> In the following we will also use the usual expression 'intensity'.

<sup>4</sup> The Digitized Sky Surveys were produced at the Space Telescope Science Institute under U.S. Government grant NAG W-2166. The images of these surveys are based on photographic data obtained using the Oschin Schmidt Telescope on Palomar Mountain and the UK Schmidt Telescope. The plates were processed into the present compressed digital form with the permission of these institutions.

**Table 3.** Summary of the VLA observations.  $t$  is the on-source observation time (in hours).  $\sigma_I$  is the rms noise in the final map of total intensity and  $\sigma_{PI}$  the rms noise in the final map of polarized intensity (both in  $\mu\text{Jy}/\text{beam}$ ). Column 5 gives only noise levels at  $\lambda 22$  cm, those at  $\lambda 18$  cm are about 30% higher.

NGC	$\lambda 22$ cm and $\lambda 18$ cm				$\lambda 6.2$ cm				$\lambda 3.5$ cm			
	Date	Conf.	$t$	$\sigma_I/\sigma_{PI}$	Date	Conf.	$t$	$\sigma_I/\sigma_{PI}$	Date	Conf.	$t$	$\sigma_I/\sigma_{PI}$
1097	96 Feb3	CnB	0.7	60/40	96 May20	DnC	0.5		96 May20			
					+98Nov13+15	CnB	9.3	40/20	+97 Oct7+9	DnC	5.6	
									+98Nov11+14	CnB	9.3	30/15
1300	–”–	CnB	1.0	50/40	96 May20	DnC	1.8	25/25	96 May20	DnC	2.0	25/20
1365	–”–	CnB	1.0	80/60	96 May20				96 May20			
					+99 Feb19	DnC	6.0	15/15	+97 Oct7+9	DnC	5.6	20/15
2336	96Mar10+22	C	1.1	25/25	96 Jul22	D	2.0	15/20	96 Jul22	D	2.2	20/–
3359	96 Mar10	C	0.4	30/25	–”–	D	0.7	30/25	–”–	D	0.9	30/35
3953	–”–	C	0.4	30/20	–”–	D	0.7	25/30	–”–	D	0.9	30/–
3992	–”–	C	0.7	30/25	96 Jul22				96 Jul22			
					+96 Aug17	D	0.7	20/20	+96 Aug17	D	0.9	40/25
4535	–”–	C	0.4	20/20	96 Aug17	D	0.5	20/20	96 Aug17			
									+99 Apr2	D	6.6	25/15
5068	97 Jun12	CnB	2.0	30/35	96 Jun1	DnC	0.8		96 Aug17	D	1.2	20/25
					+96 Aug17	D	1.1	20/15				
7479	96 Mar22				96 Jul22	D	0.5	25/30	96 Jul22			
	+97 Jul2	C	2.1	40/25					+98 Jan9+10	D	5.0	20/15

the upper left corner of each frame, dashes indicate the orientation of the observed  $E$  vector of the polarized emission turned by  $90^\circ$ . These ‘ $B$  vectors’ indicate the orientation of the magnetic field only in case of small Faraday rotation (see below). Due to missing spacings, the VLA maps at  $\lambda 3$  cm and the ATCA maps at  $\lambda 13$  cm do not show the extended emission in full.

We did not attempt to separate the thermal from the nonthermal emission because for most galaxies we have only maps at one or two wavelengths which show the full extended emission. The average thermal fraction in spiral galaxies is only  $\simeq 10\%$  at  $\lambda 20$  cm (Niklas et al. 1997) which corresponds to  $\simeq 20\%$  at  $\lambda 6$  cm and  $\simeq 30\%$  at  $\lambda 3$  cm (assuming a nonthermal spectral index of 0.85).

Figures 25 and 26 show the distribution of polarized intensity PI and the observed  $B$  vectors for the galaxies with the strongest polarization. We give the accurate observational wavelengths in the titles, but for ease of reading we will summarize all C-band observations as ‘ $\lambda 6$  cm’ and all X-band observations as ‘ $\lambda 3$  cm’. At the shorter wavelengths,  $\lambda 6$  cm and  $\lambda 3$  cm, the  $B$  vectors in the Figures show the approximate orientation of the magnetic field averaged over the beam. A correction for Faraday rotation, significant at  $\lambda \geq 13$  cm, was not attempted because of insufficient signal-to-noise ratios of the polarization data at these wavelengths.

In Section 4 we quote Faraday rotation measures (RM) between  $\lambda 22$  cm and  $\lambda 6$  cm which, however, can strongly be affected by Faraday depolarization (Sokoloff et al. 1998). RM values between  $\lambda 6$  cm and  $\lambda 3$  cm were computed only for NGC 1097 and NGC 1365 for which

the signal-to-noise ratio at  $\lambda 3$  cm is sufficiently high. Correction for Faraday rotation in the Galactic foreground was not attempted.

We note that polarized emission can also be produced by anisotropic turbulent magnetic fields (Laing 1981, Sokoloff et al. 1998, Laing 2002) which can be a result of compression and/or shearing by streaming velocities. These turbulent magnetic fields do not produce any Faraday rotation. The anisotropy of turbulence could be significant in bars. Further Faraday rotation measures with high accuracy and good resolution are required to distinguish between anisotropic turbulent and coherent regular fields in our sample galaxies.

The total and polarized intensities  $I$  and  $PI$  were integrated in concentric rings ( $15''$  wide) defined in each galaxy’s plane, using the inclination  $i$  and position angle PA given in Tables 1 and 2. The maximum radius for the integration is the outer radius of the ring where  $I$  reaches the noise level. The integrated flux density  $S_\lambda$  is given in Tables 5 and 6. The average degree of polarization  $p_\lambda$  was obtained from the integrated values of  $I$  and  $PI$ . The errors in  $S_\lambda$  and  $p_\lambda$  include (as a quadratic sum) a 5% uncertainty in the absolute flux calibration and the zero-level uncertainty. In order to determine the zero level, we calculated the average surface brightness in several rings located outside the galaxy image. The rms scatter of these averages was adopted as the zero-level uncertainty.

The variations of the radio flux density and far-infrared flux density between the galaxies of our sample cannot be explained by variations in distance alone. Having scaled the radio flux density at  $\lambda 6$  cm to a common distance of

**Table 4.** Summary of the ATCA observations.  $t$  is the on-source observation time (in hours).  $\sigma_I$  is the rms noise in the final map of total intensity and  $\sigma_{PI}$  the rms noise in the final map of polarized intensity (both in  $\mu\text{Jy}/\text{beam}$ ).

NGC	$\lambda 13\text{ cm}$				$\lambda 5.8\text{ cm}$			
	Date	Conf.	$t$	$\sigma_I/\sigma_{PI}$	Date	Conf.	$t$	$\sigma_I/\sigma_{PI}$
986					96 Jan20	750C	2	
					+96 Feb10+11	750B	3	40/25
1313					96 Jan20	750C	2	
					+96 Feb10+11	750B	2	70/25
1433					96 Jan20	750C	2	
					+96 Feb10+11	750B	2	40/25
1493					96 Jan20	750C	2	
					+96 Feb10+11	750B	2	50/25
1559	96 Oct29	1.5A	5	100/40	96 Jan20	750C	2	
					+96 Feb10+11	750B	3	
					+96 Nov1	750A	11	30/15
1672	93 May19	1.5B	10 *	60/-	92 Mar15	375	11	
					+93 Jul26	750D	10 **	
					+93 Sep9	750C	12 **	50/25
2442	96 Oct29	1.5A	5	70/60	96 Jan19	750C	3	
					+96 Feb9+11	750B	4	
					+96 Nov2	750A	10	
					+98 Mar25	375	9	
					+00 Dec31	750C	11	25/25
3059	98 Jan9	1.5A	7 *	60/60	96 Jan19	750C	3	
					+96 Feb9+11	750B	4	
					+97 Jan7	750D	6	
					+98 Apr9	750A	10	25/25
5643					96 Jan19	750C	3	
					+96 Feb9+11	750B	3	40/25
7552					96 Jan19	750C	3	
					+96 Feb9+11	750B	3	
					+99 Jan3	375	8	
					+00 Dec30	750C	7	100/25

\* Simultaneous observations at  $\lambda 22\text{ cm}$  (1380 MHz)

\*\* Simultaneous observations at  $\lambda 3.5\text{ cm}$  (8640 MHz)

10 Mpc ( $S_{6\text{cm}}^*$ , a measure of radio luminosity), we define three groups of galaxies (see Fig. 1 and column 7 of Tables 5 and 6):

- **Radio-weak:** NGC 1300, 1313, 1433, 1493, 2336, 3059, 3359, 3953, 3992, 4535, 5068 ( $S_{6\text{cm}}^* < 60\text{ mJy}$ ).
- **Moderate:** NGC 986, 1559, 1672, 2442, 5643 ( $120\text{ mJy} < S_{6\text{cm}}^* \leq 270\text{ mJy}$ ).
- **Radio-bright:** NGC 1097, 1365, 7479, 7552 ( $S_{6\text{cm}}^* > 330\text{ mJy}$ ).

Our sample is admittedly small and biased towards radio-bright galaxies. Our preliminary classification should be investigated with a larger sample in radio continuum and/or infrared emission.

The average total surface brightness  $I_{6\text{cm}}$  was computed by dividing  $S_{6\text{cm}}$  by the number of beams in the integration area. The results are given in column 11 of Tables 5 and 6. The error in  $I_{6\text{cm}}$  is dominated by the uncertainty in

the integration area which is estimated to be about 25%. A classification based on  $I_{6\text{cm}}$  is similar to that based on  $S_{6\text{cm}}^*$ .

## 4. Individual galaxies

### 4.1. The VLA sample

NGC 1097 (Fig. 5) has one of the intrinsically longest bars in our sample ( $\simeq 16\text{ kpc}$ ) and is the most interesting galaxy concerning radio polarization. The nucleus (Seyfert 1 type, Storchi-Bergmann et al. 1997) and the circumnuclear starburst ring of  $17''$  ( $\simeq 1.3\text{ kpc}$ ) radius (see Hummel et al. 1987, Gerin et al. 1988) are prominent in total radio intensity. Polarized radio emission in this region reveals a spiral magnetic field extending from the circumnuclear ring towards the centre (Beck et al. 1999). NGC 1097 also features strong polarized

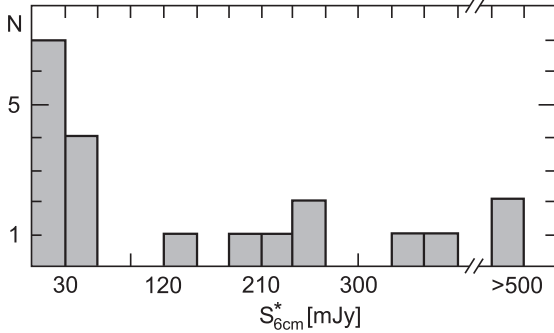


**Fig. 1.** Histogram of the total radio flux densities  $S_{6\text{cm}}^*$ , scaled to a distance of 10 Mpc, of the sample galaxies at  $\lambda 6$  cm

emission *upstream*<sup>5</sup> of the shock fronts (identified with the dust lanes offset from the bar major axis), where the regular magnetic field makes a large angle with the bar’s major axis and then, upstream of the dust lanes, turns to become aligned with the bar. This strong turning of polarization vectors leads to beam depolarization, so that the upstream regions appear as two elongated minima of polarized emission in Fig. 25. The enhancement of total and polarized emission in the dust lanes is only moderate and much weaker than the gas density enhancement (Beck et al. 1999). Extended polarized emission with apparent magnetic field orientation *perpendicular* to the optical spiral arms (Fig. 25) is visible in the northeast and southwest. The spiral arms outside the bar region exhibit only weak radio emission. Faraday rotation between  $\lambda 22$  cm and  $\lambda 6$  cm is generally weak, with  $|\text{RM}| \leq 10 \text{ rad m}^{-2}$ , except in the central region where RM varies between  $-35 \text{ rad m}^{-2}$  and  $+35 \text{ rad m}^{-2}$ . RM between  $\lambda 6$  cm and  $\lambda 3$  cm is generally higher, it varies between  $+160 \text{ rad m}^{-2}$  in the upstream region and  $-150 \text{ rad m}^{-2}$  in the downstream region of the southern bar, and between  $+200 \text{ rad m}^{-2}$  and  $-170 \text{ rad m}^{-2}$  near the centre. The increase of RM with decreasing wavelength is typical for spiral galaxies (Sokoloff et al. 1998).

*NGC 1300* (Fig. 6) has one of the most pronounced optical bars in our sample. Total radio intensity is maximum in the nuclear region and at the ends of the bar where the spiral arms start (both are sites of strong star formation). No significant radio emission has been detected in the bar. The polarized emission is weak. The northern extensions visible in the maps at  $\lambda 22$  and 6 cm are not real and result from poor data coverage in the *uv* plane. The  $\lambda 18$  cm and  $\lambda 3$  cm maps show less emission than those at  $\lambda 22$  cm and  $\lambda 6$  cm because the signal-to-noise ratios are worse.

*NGC 1365* (Fig. 7) is the intrinsically largest and radio-brightest galaxy in our sample. Its bar length is

<sup>5</sup> As the gas moves faster than the pattern speed of the bar, *upstream* is defined as the region in front of the shock which lags behind with respect to the galaxy’s rotation.

$\simeq 29$  kpc. It has a Seyfert 1-type nucleus surrounded by a starburst region (see review by Lindblad 1999). Similarly to NGC 1097, it has significant (though weaker) polarized radio emission upstream of the shock fronts and relatively weak emission enhancements on the dust lanes. The turn of magnetic field lines towards the dust lanes near the bar major axis is much smoother than in NGC 1097. The magnetic field orientations near the centre also form a spiral pattern. Sandqvist et al. (1995) describe a circumnuclear elliptical ring of about 1 kpc in radius, visible in radio continuum at  $\lambda \lambda 20$  and 6 cm at a resolution of  $2.3'' \times 1.0''$ , and note its similarity to that in NGC 1097. Kristen et al. (1997) have revealed, in the optical range, a large number of bright spots arranged along the ring and suggest that the continuous ring structure might be obscured by dust absorption. The ring is not resolved in our observations. Faraday rotation between  $\lambda 22$  cm and  $\lambda 6$  cm is significant only in the central region ( $\text{RM} \simeq -20 \text{ rad m}^{-2}$ ). RM between  $\lambda 6$  cm and  $\lambda 3$  cm jumps between  $\simeq +600 \text{ rad m}^{-2}$  and  $\simeq -600 \text{ rad m}^{-2}$  near the centre. The spiral arms outside the bar region are bright in radio and the regular magnetic field is well aligned with them (different from NGC 1097). A ridge of polarized emission (Fig. 25) is observed on the *inner* side of the northwestern spiral arm which may indicate field compression by a density wave, a ‘magnetic arm’, or depolarization along the optical spiral arm. This galaxy has an extended, almost circular, polarized envelope with the regular field aligned with the optical spiral arms.

*NGC 2336* (Fig. 8) has a small optical bar. Two extended regions of total radio emission are prominent, but they do not coincide well with star-forming regions. No emission has been detected from the bar and the nucleus. No polarization has been detected. The northern extensions at  $\lambda 18$  cm and 22 cm are probably not real but result from poor data coverage in the *uv* plane.

*NGC 3359* (Fig. 9) has enhanced total radio emission from the bar where star formation is strong as well. The total emission from the southern spiral arm peaks in star-forming regions, which are best visible at  $\lambda 6$  cm. Weak polarized emission has been detected in the *interarm* regions with field lines parallel to the adjacent optical arm. No polarized emission has been detected from the bar, possibly due to insufficient angular resolution and depolarization.

*NGC 3953* (Fig. 10) is notable for its extended, diffuse, polarized radio emission from the outer disc. No significant radio emission from the bar and the nucleus has been detected. Significant Faraday rotation between  $\lambda 22$  cm and  $\lambda 6$  cm occurs in the southern part of the galaxy ( $\text{RM} \simeq +15 \text{ rad m}^{-2}$ ).

*NGC 3992* (Fig. 11) features strong polarized radio emission from spiral arms with aligned magnetic fields. Weak emission from the nucleus has only been detected at  $\lambda 6$  cm and 3 cm (the sensitivity was too low at  $\lambda 22$  cm and 18 cm). No emission from the bar has been detected. Faraday rotation is significant ( $\text{RM} \simeq +20 \text{ rad m}^{-2}$ ) between  $\lambda 22$  cm and  $\lambda 6$  cm.

*NGC 4535* (Fig. 12) exhibits apparently unpolarized radio emission from the central region and the bar, which is small and just resolved in our images. The polarized emission mainly comes from spiral arms with aligned magnetic fields and from the northern *interarm* region (Fig. 25). Faraday rotation is weak between  $\lambda 22$  cm and  $\lambda 6$  cm ( $|\text{RM}| \leq 10 \text{ rad m}^{-2}$ ), but larger between  $\lambda 6$  cm and  $\lambda 3$  cm ( $\text{RM} \simeq +80 \text{ rad m}^{-2}$ ).

*NGC 5068* (Fig. 13) has strong radio emission from the small bar and star-forming regions. Weak polarization has been detected at  $\lambda 6$  cm in the southern part.

*NGC 7479* (Fig. 14) has strong polarized radio emission, mainly due to the nuclear ‘jet’ which was discovered by Laine & Gottesman (1998). The jet is not resolved in the maps presented here (Figs. 14 and 25). Total emission is enhanced in the western spiral arm. The polarized emission and Faraday rotation in this galaxy will be discussed in detail elsewhere.

#### 4.2. The ATCA sample

*NGC 986* (Fig. 15) has strong radio emission from the central star-forming region and the bar. Polarized emission is observed in the inner bar.

*NGC 1313* (Fig. 16) exhibits strong radio emission from the bar and star-forming regions. No polarization has been detected.

*NGC 1433* (Fig. 17) has weak radio emission from the central region which hosts an irregular star-forming ring of  $5''$  or  $\simeq 0.3 \text{ kpc}$  radius (Maoz et al. 1996). Star formation has not been detected in the bar but is noticeable in the ring-like spiral arms, in particular at the ends of the bar (see  $\text{H}\alpha$  image by Crocker et al. 1996) where weak radio emission is seen. No polarization has been detected.

*NGC 1493* (Fig. 18) shows weak radio emission from the outer spiral arms. Polarization has only been detected in a small region in the southeast.

*NGC 1559* (Fig. 19) possesses massive spiral arms with strong star formation. The small bar of about  $40''$  length is oriented almost east-west. Very strong radio emission originates in the bar and the disc. Polarized emission is strongly asymmetric with peaks near the ends of the bar and magnetic field lines at large angles to the bar (Fig. 26). The region where the magnetic field is strongly aligned and almost perpendicular to the bar’s major axis is larger than in NGC 1097.

*NGC 1672* (Fig. 20) has the second largest bar in our sample ( $\simeq 20 \text{ kpc}$ ). Its radio emission is very strong in the nucleus, the bar and the inner part of the spiral arm region. The nucleus is known to be of Seyfert 2 type and is surrounded by a starburst region (Evans et al. 1996). Polarized emission is strongest in the northeastern region *upstream* of the dust lanes, with magnetic field lines at large angles to the bar, smoothly turning towards the centre as in NGC 1097 and 1365 (Fig. 26).

*NGC 2442* (Fig. 21), a member of the Volans Group, has an asymmetric appearance which may be a result of

tidal interaction (Mihos & Bothun 1997) or ram pressure stripping (Ryder et al. 2001). The  $\text{H}\alpha$  image by Mihos & Bothun (1997) shows an unresolved central source and a circumnuclear star-forming ring of  $8''$  ( $\simeq 0.6 \text{ kpc}$ ) radius. NGC 2442 exhibits strong radio emission from the nucleus and the ends of the bar. Very strong and polarized emission has been detected in the northern arm (hosting a massive dust lane) with aligned field lines, possibly a signature of field compression and/or shearing. Diffuse radio emission is visible in the eastern part (Fig. 21), with a blob of highly polarized emission (Fig. 26). This galaxy will be discussed in Paper III (Harnett et al. 2002).

*NGC 3059* (Fig. 22) has a small optical bar. Diffuse, polarized radio emission has been detected in the whole disc, indicating a widespread, spiral, regular magnetic field similar to that of non-barred spiral galaxies. This is not surprising as the bar is small and under-resolved. We cannot exclude that this galaxy has a magnetic field component aligned with the bar.

*NGC 5643* (Fig. 23) has strong, diffuse radio emission from the nucleus, the bar and the disc. The central region and outer disc are weakly polarized with some indication of a spiral pattern.

*NGC 7552* (Fig. 24), a member of the Grus Quartet, has a starburst circumnuclear ring of  $8''$  ( $\simeq 0.8 \text{ kpc}$ ) radius, observed in radio continuum and near-infrared, a nuclear bar (observed in radio continuum and near-infrared) lying perpendicular to the primary bar, but no active nucleus (Forbes et al. 1994a,b). It is notable for strong, highly polarized radio emission from the centre, the bar and the inner parts of the spiral arms. Our resolution is insufficient to resolve the radio ring. Polarized emission is strong upstream of the dust lanes, with magnetic field lines oriented at large angles to the bar major axis (Fig. 26); these features make this galaxy similar to NGC 1097 and NGC 1672. The outer extensions in Fig. 24 are artifacts due to insufficient *uv* coverage. A detailed discussion of this galaxy will be given in Paper III.

## 5. Discussion

### 5.1. The radio–infrared correlation

The integrated  $\lambda 6$  cm radio flux density  $S_{6\text{cm}}$  (Tables 5 and 6) is correlated with the integrated  $\lambda 60 \mu\text{m}$  far-infrared flux density  $S_{60\mu\text{m}}$  (Tables 1 and 2) as shown in Fig. 2. The correlation coefficient is  $0.97 \pm 0.02$ . NGC 1559 lies well above the fitted line, i.e., its radio emission is ‘too high’ compared with its far-infrared emission (cf. Section 5.2). This is possibly also true for NGC 1097. NGC 986 and NGC 7552 are ‘too radio-faint’, possibly due to the incomplete *uv* coverage of our observations.

The radio–far-infrared correlation has been studied in detail for large samples of barred and non-barred galaxies. The average *flux density* ratio  $S_{6\text{cm}}/S_{60\mu\text{m}}$  (where  $S_{6\text{cm}}$  is measured in mJy and  $S_{60\mu\text{m}}$  in Jy) is  $3.0 \pm 0.3$  for the RC2 galaxies in the sample of de Jong et al. (1985) and  $2.3 \pm 0.1$  for the 134 galaxies observed by Unger et al. (1989, scaled

**Table 5.** The flux density  $S_\lambda$ , the flux density  $S_{6\text{cm}}^*$  scaled to a distance of 10 Mpc, the average degree of polarization  $p_\lambda$  (based on the maps at  $30''$  resolution), the average total surface brightness  $I_{6\text{cm}}$  (in mJy/beam area), the total equipartition field strength  $B_{\text{tot}}$ , and its resolved regular component  $B_{\text{reg}}$  for the VLA sample. Values in brackets are lower limits where low signal-to-noise ratios or insufficient  $uv$  coverage preclude better estimates.

NGC	$S_{22\text{cm}}$ [mJy]	$p_{22\text{cm}}$ [%]	$S_{18\text{cm}}$ [mJy]	$p_{18\text{cm}}$ [%]	$S_{6\text{cm}}$ [mJy]	$S_{6\text{cm}}^*$ [mJy]	$p_{6\text{cm}}$ [%]	$S_{3\text{cm}}$ [mJy]	$p_{3\text{cm}}$ [%]	$I_{6\text{cm}}$ [mJy/ b.a.]	$B_{\text{tot}}$ [ $\mu\text{G}$ ]	$B_{\text{reg}}$ [ $\mu\text{G}$ ]
1097	350±25	1.5±0.9	262±30	1.3±1	142±12	359	8.5±1.0	94±18	5.7±1.7	1.67	13±4	4±1
1300	29± 4	10± 3	[14]	—	11± 2	44	9± 4	5± 1	10± 5	0.19	8±2	3±1
1365	540±31	1.6±0.4	423±30	1.7±1	206±13	744	2.4±0.5	116±10	2.2±0.6	2.69	15±5	3±1
2336	13± 2	< 3	[5]	—	4.2±0.6	41	< 4	1.4±0.3	—	0.10	6±2	< 2
3359	41± 3	6± 3	[24]	—	13± 1	28	5± 3	[5]	—	0.33	8±2	2±1
3953	24± 2	2± 2	[15]	—	7± 1	16	7± 3	[2]	—	0.21	7±2	2±1
3992	12± 2	7± 6	—	—	4.5±0.8	10	11± 4	2± 1	—	0.09	6±2	2±1
4535	43± 4	9± 5	[19]	—	13± 2	33	14± 4	8± 1	8± 4	0.21	8±2	3±1
5068	43± 5	—	36± 5	—	14± 1	8	4± 2	[4]	—	0.23	8±2	2±1
7479	110± 6	4± 2	[55]	—	33± 4	379	6.5±1.5	22± 4	9± 3	0.83	11±3	3±1

**Table 6.** As in Table 5, but for the ATCA sample.

NGC	$S_{22\text{cm}}$ [mJy]	$p_{22\text{cm}}$ [%]	$S_{13\text{cm}}$ [mJy]	$p_{13\text{cm}}$ [%]	$S_{6\text{cm}}$ [mJy]	$S_{6\text{cm}}^*$ [mJy]	$p_{6\text{cm}}$ [%]	$S_{3\text{cm}}$ [mJy]	$p_{3\text{cm}}$ [%]	$I_{6\text{cm}}$ [mJy/b.a.]	$B_{\text{tot}}$ [ $\mu\text{G}$ ]	$B_{\text{reg}}$ [ $\mu\text{G}$ ]
986	—	—	—	—	38± 3	246	2± 1	—	—	0.86	12±4	2±1
1313	—	—	—	—	20± 3	3	< 3	—	—	0.37	9±3	< 2
1433	—	—	—	—	3± 1	5	< 3	—	—	0.06	6±2	< 1
1493	—	—	—	—	3± 1	4	6± 4	—	—	0.09	7±2	2±1
1559	—	—	[150]	0.3±0.1	105± 6	232	3.9±0.4	—	—	4.13	16±5	4±1
1672	[190]	—	[170]	—	106± 6	250	3.8±0.9	47± 3	5.7±1.3	1.95	14±4	3±1
2442	—	—	[65]	—	74± 4	201	2.6±0.5	—	—	1.17	13±4	2±1
3059	[45]	11±8	[16]	—	29± 2	57	7± 1	—	—	0.65	11±3	3±1
5643	—	—	—	—	64± 4	129	2± 1	—	—	0.92	13±4	2±1
7552	—	—	—	—	125±20	546	2.0±0.5	—	—	2.16	15±5	2±1

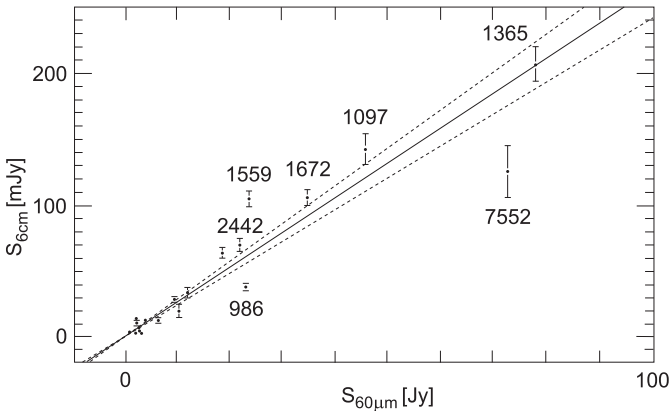


**Fig. 2.** The radio–far-infrared correlation for the sample of barred galaxies: integrated radio continuum flux density at  $\lambda 6\text{ cm}$  versus the integrated far-infrared flux density at  $\lambda 60\ \mu\text{m}$ . NGC names are indicated for bright galaxies

to  $\lambda 6\text{ cm}$ ). The slope of the fitted line in our Fig. 2 is  $2.6 \pm 0.3$ , in agreement with these results. The radio continuum *luminosity* of spiral galaxies is also closely related to the far-infrared luminosity (Condon 1992, Niklas 1997).

Unger et al. found no significant difference in the radio/far-infrared ratio either between Hubble classes or between barred and non-barred galaxies. The average value of  $S_{6\text{cm}}/S_{60\ \mu\text{m}}$  in our sample also indicates no general excess of radio emission from barred galaxies.

A close correlation between radio continuum emission and dust emission in the far-infrared has been found within many galaxies (Bicay & Helou 1990, Hoernes et al. 1998), and between radio continuum and the mid-infrared emission ( $\lambda 15\ \mu\text{m}$ ) in the spiral galaxy NGC 6946 at all spatial scales (Frick et al. 2001). ISOCAM images at  $\lambda 7\ \mu\text{m}$  and  $\lambda 15\ \mu\text{m}$  are available for several galaxies in our sample: NGC 1097, 1365, 1433, 1672, 4535 and 7552 (Roussel et al. 2001a). The similarity to our radio maps is striking and shows that the relationship holds not only for the integrated flux densities and luminosities, but also for spatial scales down to our resolution.

As synchrotron emission dominates at radio wavelengths longer than about  $\lambda 3\text{ cm}$ , the radio–infrared correlation cannot be explained solely by thermal processes. Various interpretations are discussed by Hoernes et al. (1998). As suggested by Niklas & Beck (1997), the radio–[far-]infrared correlation for bright galaxies holds if the



magnetic field is connected to the star formation rate where the gas clouds may serve as the physical link. For radio-weak galaxies, however, the far-infrared emission is dominated by cold dust heated by the general radiation field which is not related with recent star formation (Hoernes et al. 1998). Most of the galaxies in our sample are bright enough to ensure that their far-infrared emission is indeed a measure of star formation intensity.

In normal spiral galaxies, cool gas and magnetic fields are compressed in various shocks, followed by an increase in star formation. However, large-scale shock fronts in a galaxy do not always enhance star formation. For example, the non-barred spiral galaxy NGC 2276 interacts with some external (intracluster) gas, so that a large-scale shock front forms on the leading side producing a ridge of strong total and regular magnetic field without significant effect on star formation (Hummel & Beck 1995). As a consequence, this galaxy deviates from the radio-far-infrared correlation.

Barred galaxies also host large-scale shock fronts, identified with dust lanes. However, shock fronts in bars are non-standard shocks in that they have enhanced velocity shear across them, similar to bow shocks. If the shear rate  $\partial V_i/\partial x_j$  exceeds the inverse time for star formation, the gas density enhancement in the shock does not trigger star formation. If the magnetic field is compressed in the shock, the ratio of radio/far-infrared flux densities would be higher than normal. However, for our sample this ratio and the average total field strengths (Sect. 5.3) are similar to those of non-barred galaxies. This indicates that large-scale field compression in the bar is generally small and that the magnetic field is not frozen into the flow in the regions of strong compression and shear (the dust lanes). Nevertheless, the average surface brightness in radio continuum and far-infrared increases with increasing bar length (see Sect. 5.2).

## 5.2. Radio emission and bar strength

Several quantitative measures of bar strength have been suggested. Most of them are based on purely geometric parameters such as the bar axial ratio, where a smaller value of  $b/a$  means a stronger bar (Martin 1995, Aguerri 1999, Chapelon et al. 1999, Abraham & Merrifield 2000). Smallest values of  $b/a$  in our sample are found in NGC 1300, 1433, 1493, 1559, 3059, 3359 and 7552 (see Tables 1 and 2), but only NGC 1559 and NGC 7552 have a high surface brightness in radio continuum (see Tables 5 and 6) and far-infrared. NGC 1365 has the highest radio flux density  $S_{6\text{cm}}^*$  in our sample, although the aspect ratio of its bar is relatively small ( $b/a = 0.51$ ). However, it hosts the longest bar ( $\simeq 29$  kpc) in the sample. NGC 1559, 1672 and 7552 are fainter mainly because they are smaller. Their (distance-independent) radio surface brightness values  $I_{6\text{cm}}$  (measured in  $\mu\text{Jy}/\text{beam area}$ ) are similar to or even larger than that of NGC 1365 (see column 11 in Tables 5 and 6), and the same is true for the typical far-

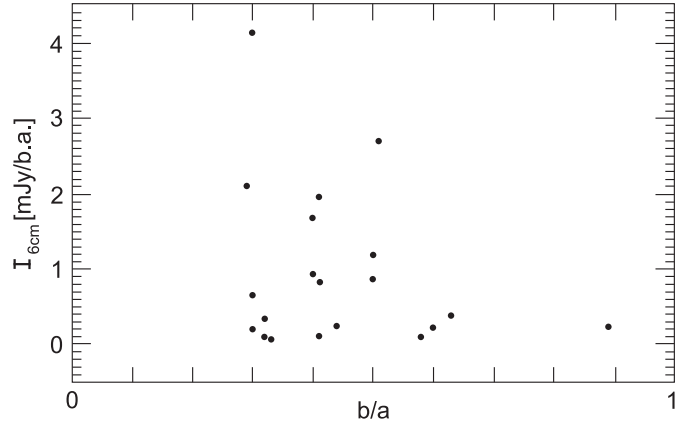


**Fig. 3.** Variation of the radio surface brightness  $I_{6\text{cm}}$  at  $\lambda 6$  cm with the deprojected aspect ratio  $b/a$  of the bar

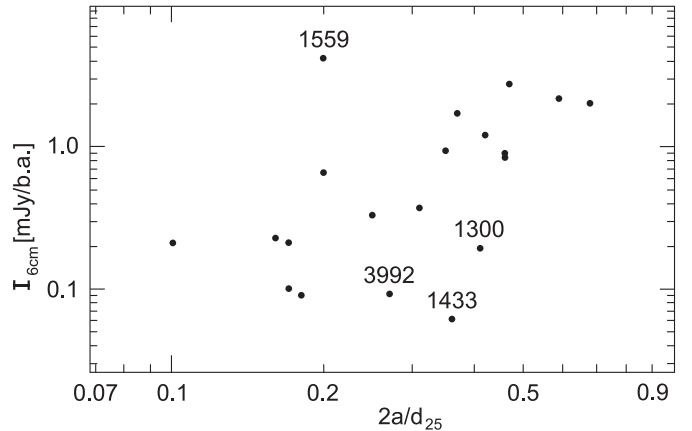


**Fig. 4.** Variation of the radio surface brightness  $I_{6\text{cm}}$  at  $\lambda 6$  cm with the relative bar length  $2a/d_{25}$  (logarithmic scales). Deviating points are marked by their NGC name

infrared surface brightness, which is a measure of star formation rate per surface area. Fig. 3 confirms that the radio surface brightness  $I_{6\text{cm}}$  is uncorrelated with the aspect ratio  $b/a$  (correlation coefficient of  $0.58 \pm 0.15$ ).

A physically motivated measure of the bar strength has been introduced by Buta & Block (2001) and Block et al. (2001) based, following Combes & Sanders (1981), on the maximum amplitude of the tangential gravitational force relative to the mean axisymmetric radial force. Thus defined, the strength parameter  $Q_b$  is sensitive not only to the bar ellipticity, but also to its size and mass, and is related to the quadrupole moment of the bar potential (P. Englmaier, priv. comm.). A reliable estimation of  $Q_b$  involves careful analysis of near-infrared galactic images (Quillen et al. 1994). Buta & Block (2001) and Block et al. (2001) determine  $Q_b$  for a selection of galaxies, but only six of them belong to our sample. Therefore, we consider a simpler (and admittedly incomplete) measure of the bar strength described in what follows.

The quadrupole moment, with respect to the major axis, of a homogeneous triaxial ellipsoid with semi-axes  $a$ ,  $b$  and  $c$  is given by  $\frac{1}{5}M(2a^2 - b^2 - c^2)$ , where  $M$  is the

mass of the ellipsoid (Landau & Lifshitz 1976). Assuming that the vertical scale height of the bar is much smaller than its size ( $c \ll a, b$ ) (e.g., Buta & Block 2001), the quadrupole moment normalized to  $M_{25}R_{25}^4$  (with  $M_{25}$  the mass within the radius  $R_{25}$ ) is given by

$$\Lambda = \left(\frac{a}{R_{25}}\right)^4 \frac{b}{a} \left(1 - \frac{1}{2} \frac{b^2}{a^2}\right) \frac{\sigma_b}{\sigma}, \quad (1)$$

where  $\sigma_b$  and  $\sigma$  are the average mass surface densities of the bar and within  $R_{25}$ , respectively, and we have omitted numerical factors of order unity. The relative bar length  $a/R_{25} = 2a/d_{25}$ , rather than the bar axial ratio, is the dominant factor in  $\Lambda$ . Moreover, 70% of galaxies in our sample have  $b/a > 0.4$ , and  $\Lambda$  varies just by 30% for  $0.4 < b/a < 1$ . Therefore,  $b/a$  is a poor measure of bar strength, especially for our sample, as it does not discriminate well enough between galaxies with  $b/a \gtrsim 0.5$ .

Since  $\Lambda$  depends strongly on the relative bar length  $2a/d_{25}$ , we can reasonably expect that radio emission is correlated with this parameter. This expectation is confirmed by the high correlation between the radio surface brightness  $I_{6\text{cm}}$  at  $\lambda 6$  cm and the relative bar length (correlation coefficient of  $0.86 \pm 0.06$ , with NGC 1559 excluded – see below), confirmed by Student’s  $t$  test. Fig. 4 shows this correlation in logarithmic scales. Although the scatter is stronger than that in Fig. 2, the correlation is not weaker than other correlations discussed for barred galaxies in the current literature (cf. Chapelon et al. 1999). We conclude that a stronger bar results in an overall enhancement of the total radio emission in the bar region despite a relatively weak compression of the regular magnetic field near the dust lanes, as discussed in Section 5.1. As noted by Block et al. (2001), longer bars can produce more extensive deviations from axial symmetry in the gas velocity because the relative tangential force is stronger when the end of the bar is farther from the (axisymmetric) bulge; this may be the physical reason for the correlation shown in Fig. 4.

With the most strongly deviating galaxy excluded (NGC 1559), the data shown in Fig. 4 can be fitted with a power law

$$I_{6\text{cm}} \propto (2a/d_{25})^{1.5 \pm 0.4}.$$

A similar dependence is valid for the far-infrared surface brightness  $I_{60\mu\text{m}}$  (exponent  $1.5 \pm 0.5$ ).

We have been unable to include the dependence on the surface mass densities into our measure of the bar strength, and this plausibly contributes into the scatter of the data points around the fit. It is difficult to say whether or not  $\sigma_b/\sigma$  is correlated with  $2a/d_{25}$ . If  $\sigma_b/\sigma$  is independent of  $2a/d_{25}$ , the above fit implies an approximate scaling

$$I_{6\text{cm}} \propto \Lambda^{0.4 \pm 0.1}.$$

There are a few deviations from the above correlation (see Fig. 4). NGC 1559 has the largest ratio of radio to far-infrared flux densities and the highest radio surface bright-

ness, and so deviates strongly from the radio–infrared correlation as well (see Fig. 2). NGC 1559 is not a member of any group or cluster of galaxies and has no nearby companion (Zaritsky et al. 1997). High-resolution radio and optical observations are required.

On the other hand, NGC 1300, 1433 and 3992 are radio-weak in spite of their relatively long bars (Fig. 4). Their far-infrared flux density and thus their star formation rate is low. Apart from an usually small value of  $\sigma_b/\sigma$  for these galaxies, other reasons for these deviations are conceivable. Martinet & Friedli (1997) argue that some galaxies with strong bars have settled into a quiescent state after an episode of vigorous star formation which has transformed most of the gas into stars. Alternatively, Tubbs (1982) and Reynaud & Downes (1998) found indications for suppression of star formation in fast flows of the gas along the bar. The field strength should be low in the first case, because there is not enough gas to hold the field or the dynamo is not able to maintain a strong magnetic field. In the second case the field should be strong, but the galaxy does not host enough cosmic-ray electrons to generate strong synchrotron radiation. This can be verified by comparing regular magnetic field strengths deduced from Faraday rotation and polarized intensity from further radio observations with higher sensitivity.

Measurements of the star formation efficiency SFE may also help: In the first case, the content of molecular gas should be low, with a SFE similar to that in spiral galaxies, while in the second case the SFE should be exceptionally small. Existing data seem to favour a *higher* SFE in barred galaxies compared to non-barred ones (Young 1993), but the infrared luminosity is dominated by the central region where star formation is triggered by gas inflow (see Roussel et al. 2001b). The SFE in the bar itself (and its possible suppression by a fast gas flow) should be subject to future investigations.

### 5.3. Magnetic field strength

The estimates of the total magnetic field strength in our Galaxy, derived from  $\gamma$ -ray data and the local cosmic-ray energy density (Strong et al. 2000), agree well with equipartition values from radio continuum data (Berkhuijsen, in Beck 2001), so that the equipartition assumption is a useful estimate, at least on scales of more than a few kpc.

From the integrated flux density  $S_{6\text{cm}}$  at  $\lambda 6$  cm and the solid angle of the integration area, the surface brightness  $I_{6\text{cm}}$  and the corresponding equipartition strength of the *total* magnetic field  $B_{\text{tot}}$  were computed (Tables 5 and 6), assuming for all galaxies a thermal contribution to the surface brightness at  $\lambda 6$  cm of 20% and a spectral index  $\alpha_n$  of the nonthermal emission of 0.85, which is the mean value for spiral galaxies of type Sb and later (Niklas et al. 1997).

Spectral indices  $\alpha$  between  $\lambda 22$  cm and  $\lambda 6$  cm ( $S_\nu \propto \nu^{-\alpha}$ ) can be computed from our VLA data (given in

Table 5). The values lie in the range 0.71 and 0.97 which is in the range typical of normal spiral galaxies (Niklas 1995). Nonthermal spectral indices  $\alpha_n$  cannot be determined with data at only two frequencies.

We adopted the standard cosmic-ray proton-to-electron ratio  $K$  of 100, a pathlength through the disc of  $1 \text{ kpc}/|\cos i|$ , and assumed that the regular field is in the galaxy's plane and the random field is statistically isotropic. Uncertainties in any of these parameters of  $\leq 50\%$  lead to an error of  $\leq 13\%$  in  $B_{\text{tot}}$ . We estimate the total error in  $B_{\text{tot}}$  to be about 30%. The relative errors between galaxies are smaller because some of the input parameters (e.g. the proton-to-electron ratio) are not expected to vary strongly from one galaxy to another.

With the above assumptions,  $B_{\text{tot}}$  is related to the average synchrotron volume emissivity  $\epsilon$  and surface brightness  $I$  (neglecting a term weakly varying with inclination  $i$ ) by

$$B_{\text{tot}} \propto \epsilon^{1/(\alpha_n+3)} \quad (\text{where } \epsilon \propto I|\cos i|).$$

Note that the equipartition field strengths are about 10% larger than the field strengths derived from the standard minimum-energy formula (which should be used with caution, see Beck 2000).

The average total magnetic field strength  $B_{\text{tot}}$ , according to Tables 5 and 6 (representing the average synchrotron emissivity), is a function of neither Hubble type (SBb–SBc) nor luminosity class (I–III), which has also been found for a much larger sample of barred and non-barred spiral galaxies (Hummel 1981). The average total field strength  $B_{\text{tot}}$  is  $10 \pm 3 \mu\text{G}$  for our sample, similar to the average minimum-energy field strength of  $\simeq 8 \mu\text{G}$  for the large galaxy sample (Hummel et al. 1988) and to the mean equipartition value of  $11 \pm 4 \mu\text{G}$  of the sample of 146 late-type galaxies calculated by Fitt & Alexander (1993), corrected to  $K = 100$ . Niklas (1995) derived a mean equipartition value of  $9 \pm 3 \mu\text{G}$  for his sample of 74 spiral galaxies. Hummel (1981) also found no significant emissivity difference between barred and non-barred galaxies.

The following galaxies have the strongest total magnetic field in our sample, as evidenced by their high radio surface brightness: NGC 1365, 1559, 1672 and 7552 (see Tables 5 and 6). This indicates that the total field strength is highest for galaxies with the (relatively) longest bars, with the exception of NGC 1559 that has a short bar (see Fig. 4).

The last column in Tables 5 and 6 gives the average equipartition strength  $B_{\text{reg}}$  of the *resolved regular* magnetic field, derived from the polarized surface brightness averaged over the galaxy.  $B_{\text{reg}}$ , in contrast to  $B_{\text{tot}}$ , depends on the linear resolution within a galaxy and thus on its physical size, its distance and its inclination. However,  $p_\lambda$  and  $B_{\text{reg}}$  in Tables 5 and 6 do not correlate with distance of the galaxy. As a test, we smoothed the  $\lambda 6 \text{ cm}$  map of NGC 1097 by enlarging the beam size from  $30''$  to  $60''$  and to  $90''$  which corresponds to increasing the galactic distance by factors 2 and 3. The degree of polarization

decreased from 8.5% to 7% and 6%, respectively, and the strength of the resolved regular magnetic field decreased from 4.3 to 4.0 and  $3.6 \mu\text{G}$ , respectively, remaining above the sample average. Hence the values of  $p_\lambda$  and  $B_{\text{reg}}$  in Tables 5 and 6 seem to depend only weakly on distance to the galaxies, implying that our observations generally resolve most of the structure in the regular magnetic field, at least for large galaxies and at distances of up to about 40 Mpc.

Average polarized surface brightness (and thus  $B_{\text{reg}}$ ) values are similar for the galaxies of our sample. The exceptions are NGC 1097 and NGC 1559 with  $B_{\text{reg}} \simeq 4 \mu\text{G}$ , above the average of  $2.5 \pm 0.8 \mu\text{G}$ . NGC 1097 probably drives a strong dynamo where field amplification is supported by shear in the velocity field (Moss et al. 2001, Paper II). The degree of polarization at  $\lambda 6 \text{ cm}$ , signature of the degree of uniformity of the resolved field, is also high in NGC 1097 (see Fig. 25). NGC 1559, 1672 and 7552 are similar candidates for a strong dynamo, but the present radio observations (Fig. 26) have insufficient linear resolution at the relatively large distances of these galaxies to reveal the true strength of the regular fields and their detailed structure.

NGC 1300, NGC 3992 and NGC 4535 have the highest degrees of polarization but only low total surface brightness. They host weak but ordered magnetic fields with spiral patterns, similar to those in non-barred galaxies (Beck 2000).

#### 5.4. Bars and global magnetic field structure

A classification system of barred galaxies was introduced by Martinet & Friedli (1997), based on the axis ratio  $b/a$  (see Tables 1 and 2) and on the star formation rate (SFR) measured by the far-infrared luminosity. Galaxies with large  $b/a$  are generally weak in star formation (class I), but some have a high SFR (class II). Galaxies with small  $b/a$  have a large spread in SFR: from high (class III) to weak (class IV). Galaxies of class IV in Martinet & Friedli have strong bars, but low SFR (see Sect. 5.2).

Here we propose that there are basic differences among barred galaxies concerning their magnetic field structure and strength which may reflect physical properties of barred galaxies like the gas flow, the shock strength in the bar and the presence of a circumnuclear ring.

Firstly, barred galaxies can have low radio luminosity because they are small (NGC 1313, 1493 and 5068), or because their gas content and star formation activity is small in spite of their large bars (NGC 1300 and 1433). Little or no polarization is detected in these galaxies. In galaxies with small bars the radio continuum morphology is formed as a result of star formation in the spiral arms, as in NGC 2336, 3359, 3953, 3992, 4535, 5643, and also M83 observed previously by Beck (2000). The bar is of little importance for the overall radio properties of these galaxies. The average degree of radio polarization (i.e., the degree of field regularity) seems to be controlled by the spiral struc-

ture rather than the bar, being low in flocculent spirals and high when massive spiral arms are present. Regular fields are often enhanced in *interarm* regions between optical spiral arms, e.g. in NGC 3359, NGC 4535 and M83, similar to non-barred galaxies.

Secondly, galaxies with long bars and strong star formation have a high radio luminosity and a strong total magnetic field ( $B_{\text{tot}} \geq 10 \mu\text{G}$ ) (NGC 1097, 1365, 1672, 2442 and 7552, and also NGC 3627 observed previously by Soida et al. 2001). NGC 1097, 1365, 1672 and 7552 have a high polarization surface brightness and a strong regular field which is enhanced *upstream* of the shock fronts in the bar. The magnetic field lines upstream of the dust lanes are oriented at large angles with respect to the bar and turn smoothly towards the dust lanes along the major axis of the bar. This is accompanied by large-scale field enhancements associated with, e.g., strong shear in the velocity field and/or strong dynamo action rather than enhanced gas density. Gas inflow along the bar may lead to circumnuclear rings which have been detected already in NGC 1097 (Hummel et al. 1987, Gerin et al. 1988), NGC 2442 (Mihos & Bothun 1997), NGC 7552 (Forbes et al. 1994a, 1994b) and possibly in NGC 1365 (Sandqvist et al. 1995), and should be searched for in the other radio-bright galaxies.

NGC 7479 is anomalous in the radio range as it possesses a nuclear ‘jet’ (Laine & Gottesman 1998). Indications of a weaker nuclear jet have been found in NGC 1365 by Sandqvist et al. (1995).

For NGC 986, 1559 and 3059 the resolution and sensitivity of the present observations are insufficient to reveal their detailed field structure.

NGC 7552 is a special case. Its radio surface brightness is high (i.e., the total magnetic field is strong, see Table 6), but still too low to be consistent with its far-infrared flux density (see Fig. 2). NGC 7552 hosts a starburst ring and may drive a ‘galactic superwind’ (Forbes et al. 1994a). As a member of a galaxy group, it may be subject to tidal interactions. It seems possible that the magnetic field is still not strong enough to hold the large number of cosmic-ray electrons produced due to the high star formation activity. However, major distortions of our radio map by instrumental effects cannot be excluded. Further radio observations are required.

## 6. Conclusions

We observed a sample of 20 barred galaxies with the VLA and ATCA radio telescopes. Polarized radio emission was detected in 17 galaxies.

The flux densities in the radio continuum and the far-infrared spectral ranges are closely correlated in our sample. The average radio/far-infrared flux density ratio and equipartition strength of the total magnetic field are similar to those in non-barred galaxies. These properties are apparently connected to the star formation rate and possibly controlled by the density of cool gas. Radio surface brightness and present star formation activity are high-

est for galaxies with a high content of molecular gas and long bars where the velocity field is distorted over a large volume. The radio surface brightness is correlated with a newly introduced measure of bar strength proportional to the quadrupole moment of the gravitational potential. However, a few galaxies with strong bars are not radio bright, possibly because their molecular gas has been depleted in a star formation burst.

In barred galaxies with low or moderate radio surface brightness, the regular field (traced by the polarized radio emission) is strongest between the optical spiral arms (e.g. NGC 3359 and 4535) or has a diffuse distribution (e.g. NGC 3059 and 3953). In radio-bright galaxies, the pattern of the regular field can, however, be significantly different: the regular magnetic field may have a broad local maximum in the bar region upstream of the dust lanes, and the field lines are oriented at large angles with respect to the bar (NGC 1097, 1365, 1672 and 7552). We propose that shear in the velocity field around a large bar may enhance dynamo action and explain the observed strong regular fields. Strong bar forcing induces shear in the velocity field and enhancements in the regular magnetic field, and polarized emission traces such shear motions.

The southern galaxies NGC 986, 1559, 1672 and 7552 show strong polarization and are promising candidates for further studies with high resolution. Circumnuclear rings are already known to exist in NGC 1097, NGC 1365, NGC 2442 and NGC 7552 and should be searched for in NGC 986, 1559 and 1672.

*Acknowledgements.* The authors would like to express special thanks to Dr. Elly Berkhuijsen for critical reading of the manuscript and many useful suggestions. Useful discussions with Drs. Peter Englmaier and David Moss are gratefully acknowledged. ME is grateful to the ATNF for providing support and facilities. His work in Australia was funded through grant No. Eh 154/1-1 from the Deutsche Forschungsgemeinschaft. VS acknowledges financial support from the RFBR/DFG programme no. 96-02-00094G and from the Royal Society. DDS acknowledges financial support from the RFBR programme no. 01-02-16158. JIH acknowledges the Australian Academy of Science for financial support under their Scientific Visits to Europe Program and the Alexander von Humboldt Foundation for its support. VS, JIH, AS and DS are grateful to the MPIfR for support and hospitality. This work was supported by the PPARC Grant PPA/G/S/1997/00284, the NATO Collaborative Linkage Grant PST.CLG 974737 and the University of Newcastle (Small Grants Panel). This work benefited from the use of NASA’s Astrophysics Data System Abstract Service.

## References

- Abraham, R. G., & Merrifield, M. R. 2000, *AJ*, 120, 2835
- Aguerri, J. A. L. 1999, *A&A*, 351, 43
- Athanassoula E. 1992, *MNRAS* 259, 345
- Beck, R. 2000, *Phil. Trans. R. Soc. Lond. A*, 358, 777
- Beck, R. 2001, in *The Astrophysics of Galactic Cosmic Rays*, eds. R. Diehl, R. Kallenbach, E. Parizot, & R. von Steiger, *Space Sci. Rev.*, 99, 243 (Dordrecht: Kluwer)

- Beck, R., & Hoernes, P. 1996, *Nature*, 379, 47
- Beck, R., Brandenburg, A., Moss, D., Shukurov, A., & Sokoloff, D. 1996, *ARA&A*, 34, 155
- Beck, R., Ehle, M., Shoutenkov, V., Shukurov, A., & Sokoloff, D. 1999, *Nature*, 397, 324
- Bicay, M. D., & Helou, G. 1990, *ApJ*, 362, 59
- Block, D. L., Puerari, I., Knapen, J. H., et al. 2001, *A&A*, 375, 761
- Buta, R., & Block, D. L. 2001, *ApJ*, 550, 243
- Chapelon, S., Contini, T., & Davoust, E. 1999, *A&A*, 345, 81
- Chiba, M., & Lesch, H. 1994, *A&A*, 284, 731
- Combes, F., & Sanders, R. H. 1981, *A&A*, 96, 164
- Condon, J. J. 1987, *ApJS*, 65, 485
- Condon, J. J. 1992, *ARA&A*, 30, 575
- Crocker, D. A., Baugus, P. D., Buta, R. 1996, *ApJS*, 105, 353
- de Jong, T., Klein, U., Wielebinski, R., & Wunderlich, E. 1985, *A&A*, 147, L6
- de Vaucouleurs, G., de Vaucouleurs, A., Corwin, H. G., et al. 1991, *Third Reference Catalogue of Bright Galaxies* (New York: Springer)
- Elmegreen, B. G., & Elmegreen, D. M. 1985, *ApJ*, 288, 438
- Evans, I. N., Koratkar, A. P., Storchi-Bergmann, T., et al. 1996, *ApJS*, 105, 93
- Fitt, A. J., & Alexander, P. 1993, *MNRAS*, 261, 445
- Forbes, D. A., Norris, R. P., Williger, G. M., & Smith, R. C. 1994a, *AJ*, 107, 984
- Forbes, D. A., Kotilainen, J. K., & Moorwood, A. F. M. 1994b, *ApJ*, 433, L13
- Frick, P., Beck, R., Berkhuijsen, E. M., & Patrickeyev, I. 2001, *MNRAS*, 327, 1145
- Fullmer, L., & Lonsdale, C. 1989, *Cataloged Galaxies and Quasars Observed in the IRAS Survey, Version 2*, JPL D-1932 (Pasadena: JPL)
- García-Barreto, J. A., Carrillo, R., Klein, U., & Dahlem, M. 1993, *Rev. Mex. Astron. Astrofis.*, 25, 31
- Gerin, M., Nakai, N., & Combes, F. 1988, *A&A*, 203, 44
- Harnett, J. I., Ehle, M., Beck, R., Thierbach, M., Haynes, R.F. 2002, in prep. (**Paper III**)
- Hoernes, P., Berkhuijsen, E. M., & Xu, C. 1998, *A&A*, 334, 57
- Hummel, E. 1981, *A&A*, 93, 93
- Hummel, E., & Beck, R. 1995, *A&A*, 303, 691
- Hummel, E., van der Hulst, J. M., & Keel, W. C. 1987, *A&A*, 172, 32
- Hummel, E., Davies, R. D., Wolstencroft, R. D., van der Hulst, J. M., & Pedlar, A. 1988, *A&A*, 199, 91
- Jörsäter, S., & van Moorsel, G. A. 1995, *AJ*, 110, 2037
- Kristen, H., Jörsäter, S., Lindblad, P. O., & Boksenberg, A. 1997, *A&A*, 328, 483
- Laine, S., & Gottesman, S. T. 1998, *MNRAS*, 297, 1041
- Laing, R. 1981, *ApJ*, 248, 87
- Laing, R. 2002, *MNRAS*, 329, 417
- Landau, L. D., & Lifshitz, E. M. 1976, *The Classical Theory of Fields*, §41 (Oxford: Pergamon)
- Lindblad, P. O. 1999, *A&A Rev*, 9, 221
- Ma, J., Peng, Q.-H., Chen, R., Ji, Z.-H., & Tu, C.-P. 1997, *A&AS*, 126, 503
- Ma, J., Peng, Q.-H., & Gu, Q.-S. 1998, *A&AS*, 130, 449
- Macri, L. M., Huchra, J. P., Stetson, P. B., et al. 1999, *ApJ*, 521, 155
- Madore, B. F., Freedman, W. L., Silbermann, N., et al. 1998, *Nature*, 395, 47
- Maoz, D., Barth, A. J., Sternberg, A., et al. 1996, *AJ*, 111, 2248
- Martin, P. 1995, *AJ*, 109, 2428
- Martin, P., & Friedli, D. 1997, *A&A*, 326, 449
- Martinet, L., & Friedli, D. 1997, *A&A*, 323, 363
- Mestel, L., & Subramanian, K. 1991, *MNRAS*, 248, 677
- Mihos, J. C., & Bothun, G. D. 1997, *ApJ*, 481, 741
- Möllenhoff, C., & Heidt, J. 2001, *A&A*, 368, 16
- Moss, D., Korpi, M., Rautiainen, P., & Salo, H. 1998, *A&A*, 329, 895
- Moss, D., Shukurov, A., Sokoloff, D., Beck, R., & Fletcher, A. 2001, *A&A*, 380, 55 (**Paper II**)
- Neininger, N., Klein, U., Beck, R., & Wielebinski, R. 1991, *Nature*, 352, 781
- Niklas, S. 1995, PhD Thesis, University of Bonn
- Niklas, S. 1997, *A&A*, 322, 29
- Niklas, S., & Beck, R. 1997, *A&A*, 320, 54
- Niklas, S., Klein, U., & Wielebinski, R. 1997, *A&A*, 322, 19
- Ondrechen, M. P. 1985, *AJ*, 90, 1474
- Ondrechen, M. P., & van der Hulst, J. M. 1983, *ApJ*, 269, L47
- Ondrechen, M. P., van der Hulst, J. M., & Hummel, E. 1989, *ApJ*, 342, 39
- Quillen, A. C., Frogel, J. A., & González, R. A. 1994, *ApJ*, 437, 162
- Reynaud, D., & Downes, D. 1998, *A&A*, 337, 671
- Rohde, R., Beck, R., & Elstner, D. 1999, *A&A*, 350, 423
- Roussel, H., Vigroux, L., Bosma, A., et al. 2001a, *A&A*, 369, 473
- Roussel, H., Sauvage, M., Vigroux, L., et al. 2001b, *A&A*, 372, 406
- Ryder, S. D., Koribalski, B., Staveley-Smith, L., et al. 2001, *ApJ*, 555, 232
- Sandage, A., & Tammann, G. A. 1981, *A Revised Shapley-Ames Catalog of Bright Galaxies* (Washington: Carnegie Inst.)
- Sandqvist, A., Jörsäter, S., & Lindblad, P. O. 1995, *A&A*, 295, 585
- Soida, M., Urbanik, M., Beck, R., Wielebinski, R., & Balkowski, C. 2001, *A&A*, 378, 40
- Sokoloff, D.D., Bykov, A.A., Shukurov, A., Berkhuijsen, E.M., Beck, R., & Poezd, A.D. 1998, *MNRAS*, 299, 189. Erratum: 1999, *MNRAS*, 303, 207
- Storchi-Bergmann, T., Eracleous, M., Ruiz, M. T., Livio, M., Wilson, A. S., & Filippenko, A. V. 1997, *ApJ*, 489, 87
- Strong, A. W., Moskalenko, I. V., & Reimer, O. 2000, *ApJ*, 537, 763
- Tubbs, A. D. 1982, *ApJ*, 255, 458
- Unger, S. W., Wolstencroft, R. D., Pedlar, A., et al. 1989, *MNRAS*, 236, 425
- Whiteoak, J. B. 1970, *Astrophys. Lett.*, 5, 29
- Wilke, K., Möllenhoff, C., & Matthias, M. 2000, *A&A*, 361, 507
- Young, J. S. 1993, in *Star Formation, Galaxies and the Interstellar Medium*, eds. J. Franco, F. Ferrini & G. Tenorio-Tagle (Cambridge: Univ. Press), 318
- Young, J. S., Xie, S., Kenney, J. D. P., & Rice, W. L. 1989, *ApJS*, 70, 699
- Zaritsky, D., Smith, R., Frenk, C., & White, S. D. M. 1997, *ApJ*, 478, 39

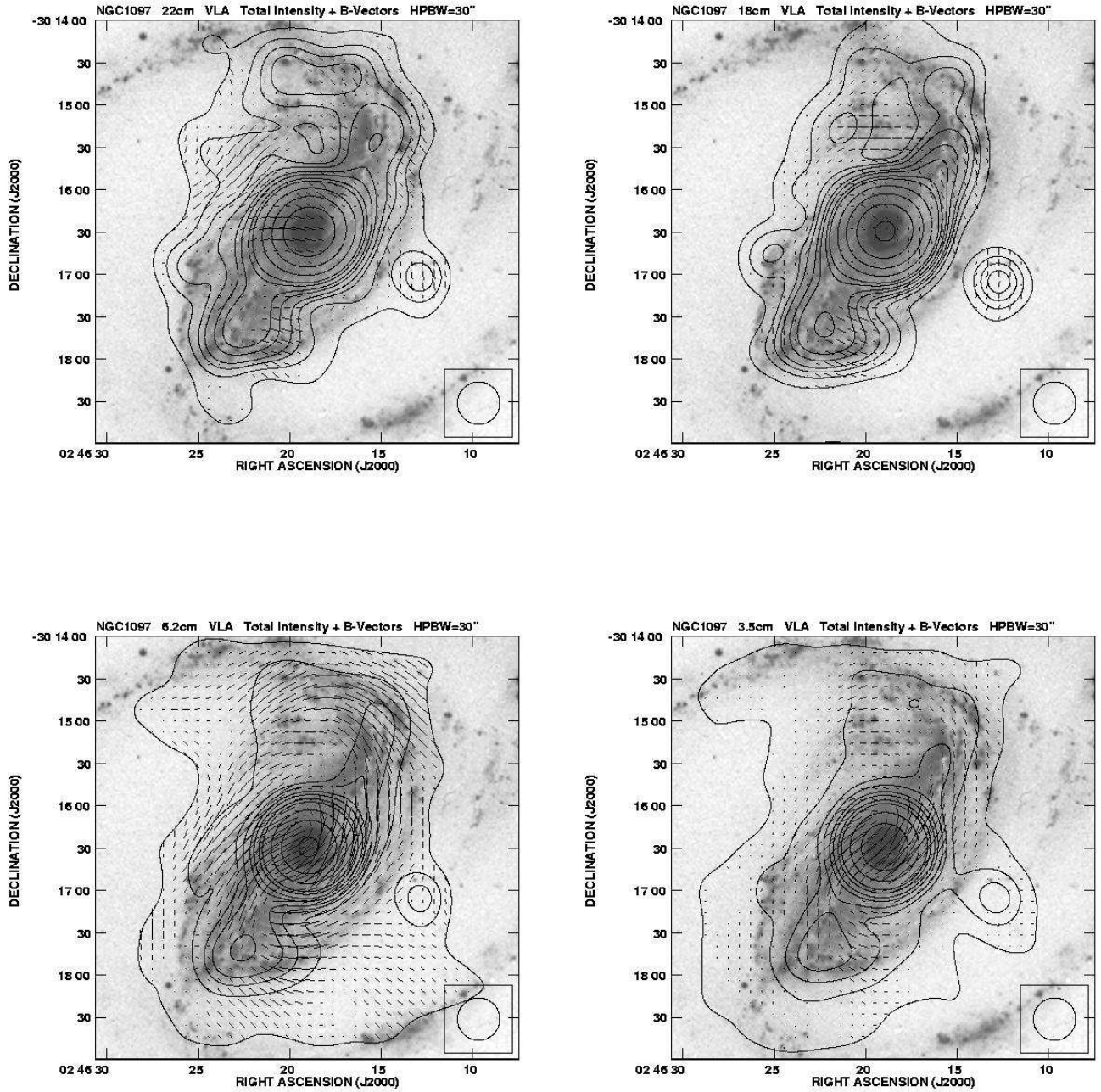


**Fig. 5.** Total intensity contours and the observed  $B$ -vectors of polarized intensity ( $E$ -vectors turned by  $90^\circ$ , uncorrected for Faraday rotation) of NGC 1097, overlaid onto an optical image kindly provided by H. Arp. The contour intervals are at 1, 2, 3, 4, 6, 8, 12, 16, 32, 64, 128,  $256 \times$  the basic contour level which is 700, 500, 500 and  $400 \mu\text{Jy}/\text{beam}$  area at  $\lambda 22$ , 18, 6.2 and 3.5 cm, respectively. A vector of  $1''$  length corresponds to a polarized intensity of  $20 \mu\text{Jy}/\text{beam}$  area. The half-power width of the synthesized beam is shown in the corner of each panel.

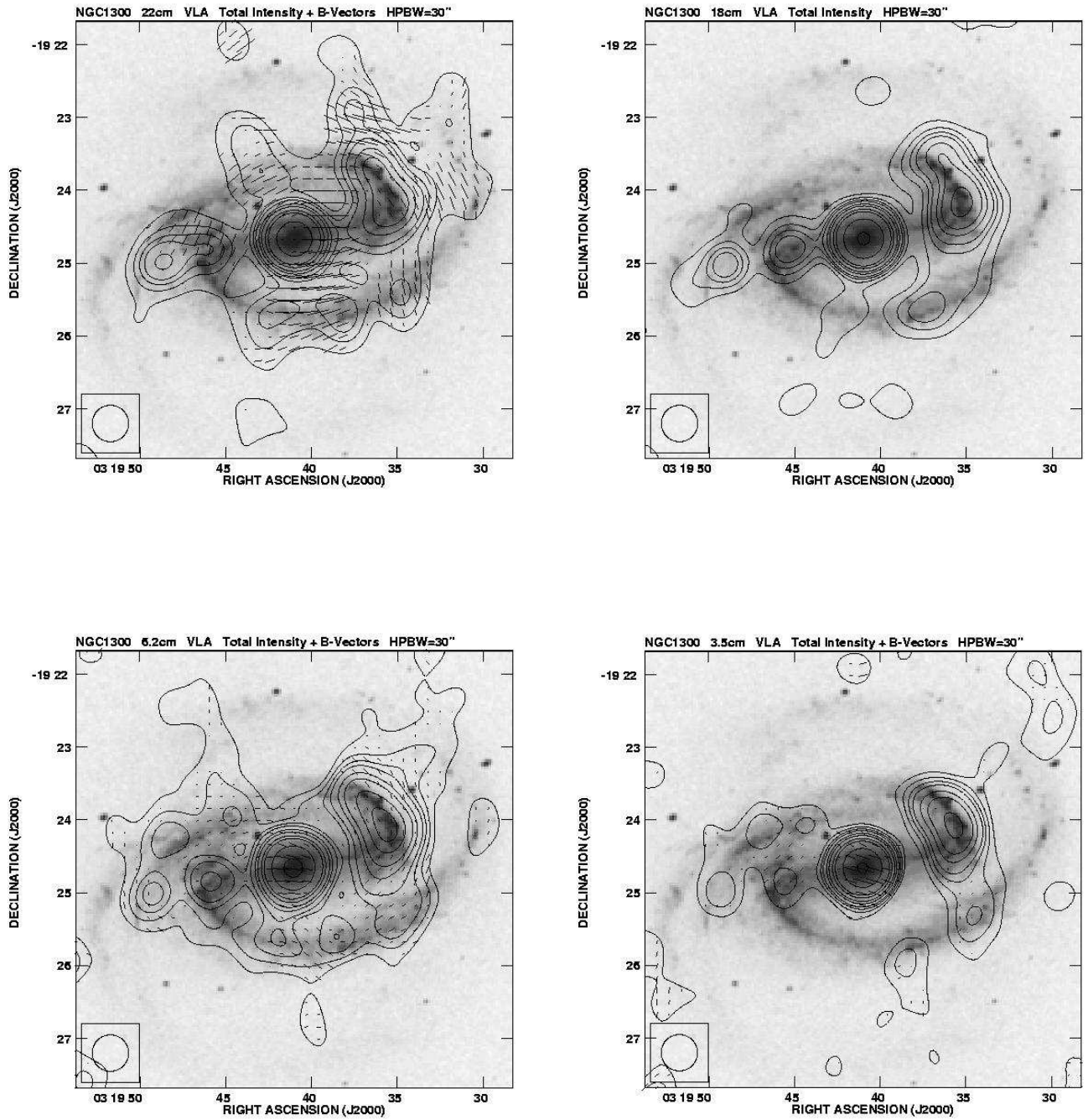


**Fig. 6.** Total intensity contours and the observed  $B$ -vectors of polarized emission of NGC 1300, overlaid onto an optical image from the Digitized Sky Surveys. The contour intervals are 1, 2, 3, 4, 6, 8, 12, 16, 32, 64, 128, 256  $\times$  the basic contour level, which is 150, 100, 50 and 40  $\mu\text{Jy}/\text{beam area}$  at  $\lambda_{22}$ , 18, 6.2 and 3.5 cm, respectively. A vector of 1" length corresponds to a polarized intensity of 10  $\mu\text{Jy}/\text{beam area}$ .

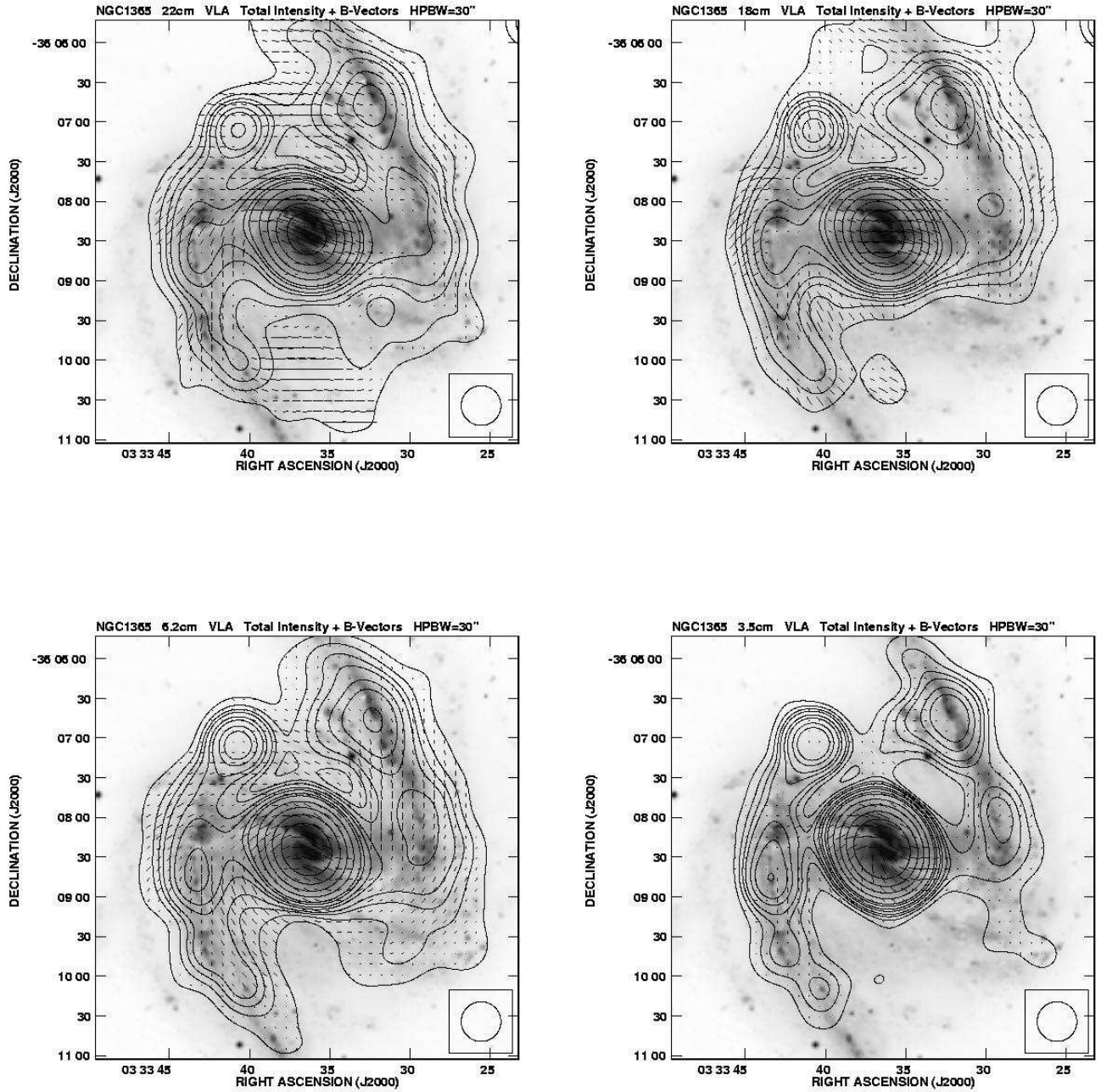


**Fig. 7.** Total intensity contours and the observed  $B$ -vectors of polarized emission of NGC 1365, overlaid onto an optical image taken at the ESO 3.6m telescope by P.O. Lindblad (1999). The basic contour levels are 700, 500, 200 and 100  $\mu\text{Jy}/\text{beam}$  area in decreasing wavelength order, the contour intervals are as in Fig. 5. A vector of 1'' length corresponds to a polarized intensity of 20  $\mu\text{Jy}/\text{beam}$  area.



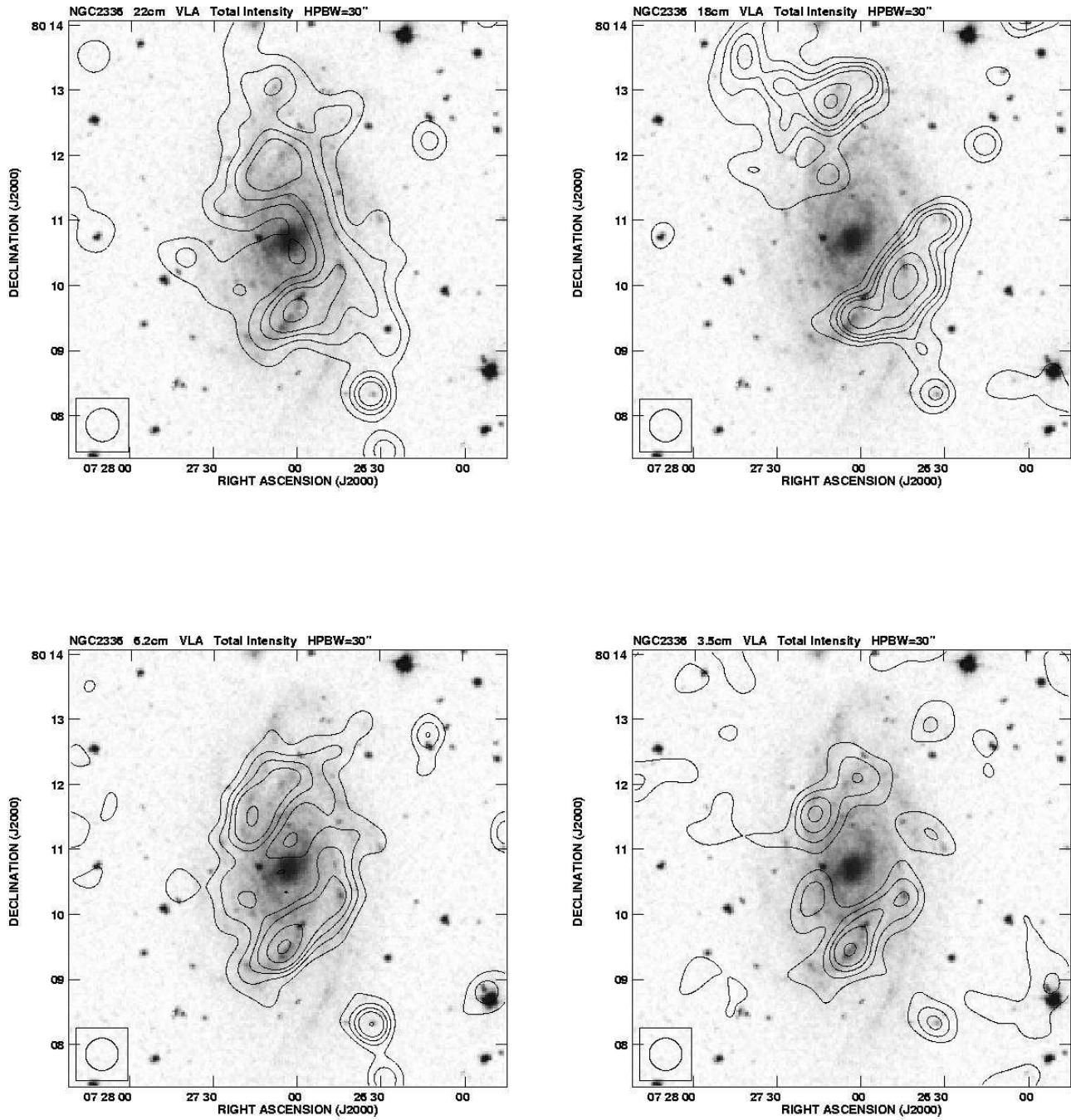


**Fig. 8.** Total intensity contours of NGC 2336, overlaid onto an optical image from the Digitized Sky Surveys. The contours are as in Fig. 6.

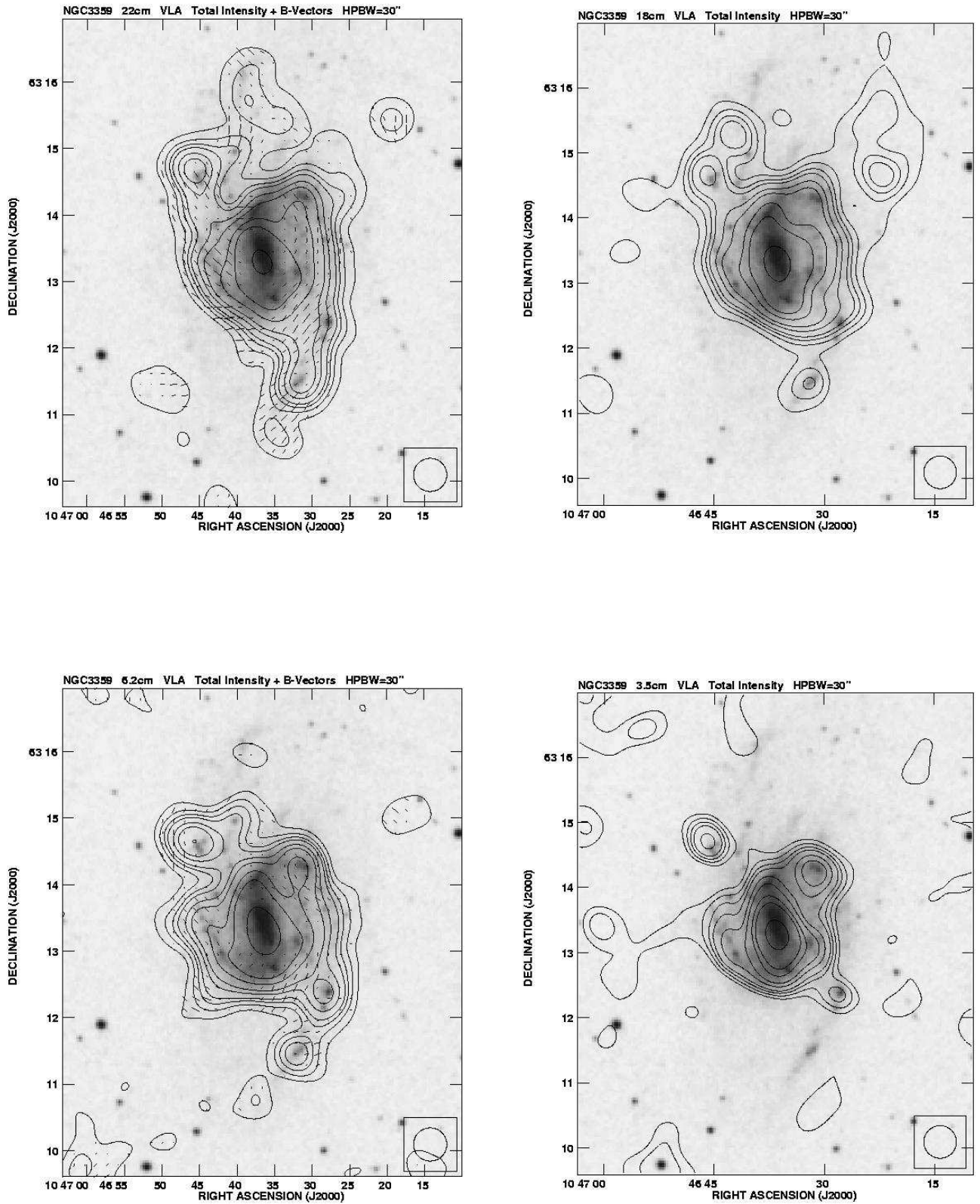


**Fig. 9.** Total intensity contours and the observed  $B$ -vectors of polarized emission of NGC 3359, overlaid onto an optical image from the Digitized Sky Surveys. The contours and the vector scale are as in Fig. 6.

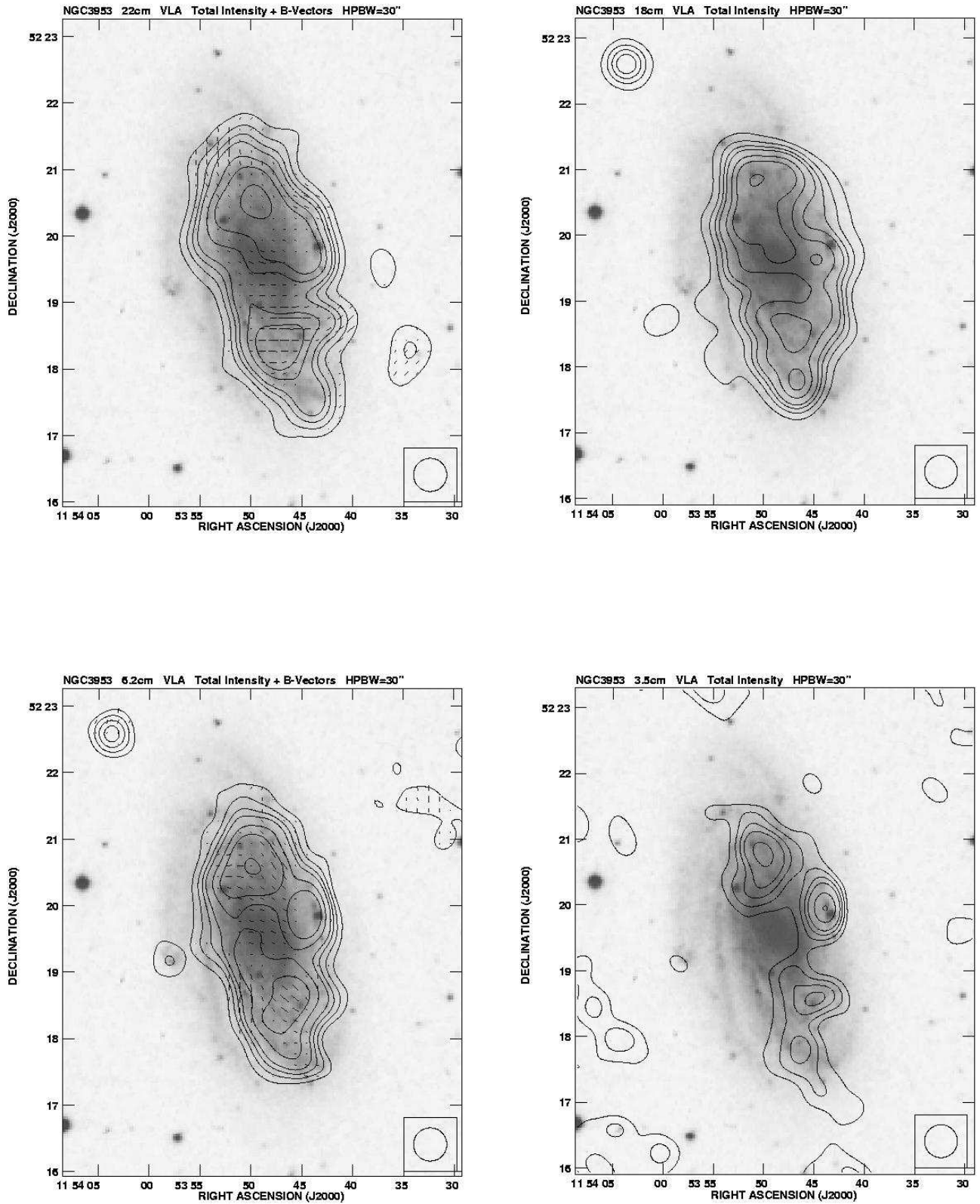


**Fig. 10.** Total intensity contours and the observed  $B$ -vectors of polarized emission of NGC 3953, overlaid onto an optical image from the Digitized Sky Surveys. The contours and the vector scale are as in Fig. 6.

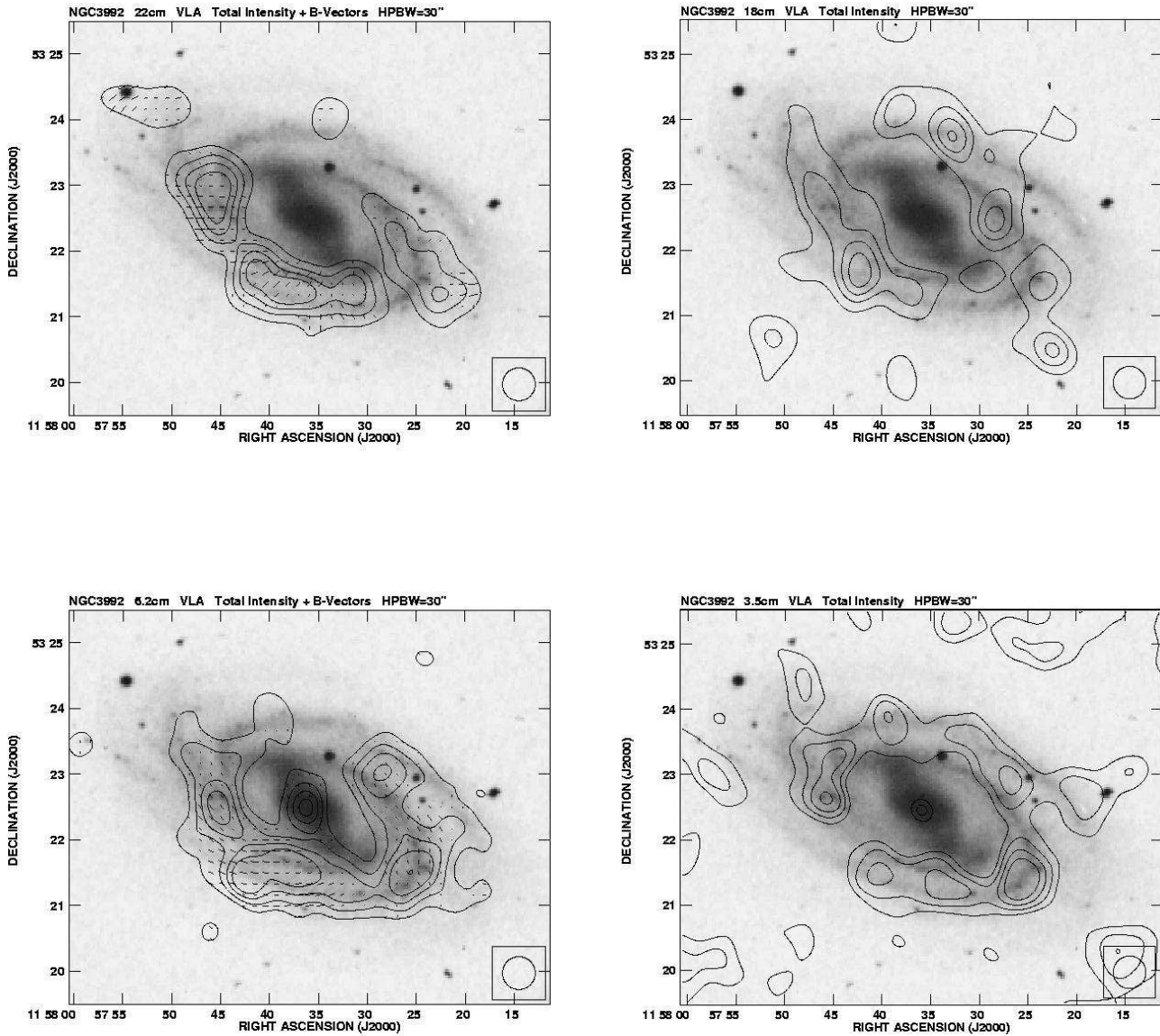


**Fig. 11.** Total intensity contours and the observed  $B$ -vectors of polarized emission of NGC 3992, overlaid onto an optical image from the Digitized Sky Surveys. The contours and the vector scale are as in Fig. 6.

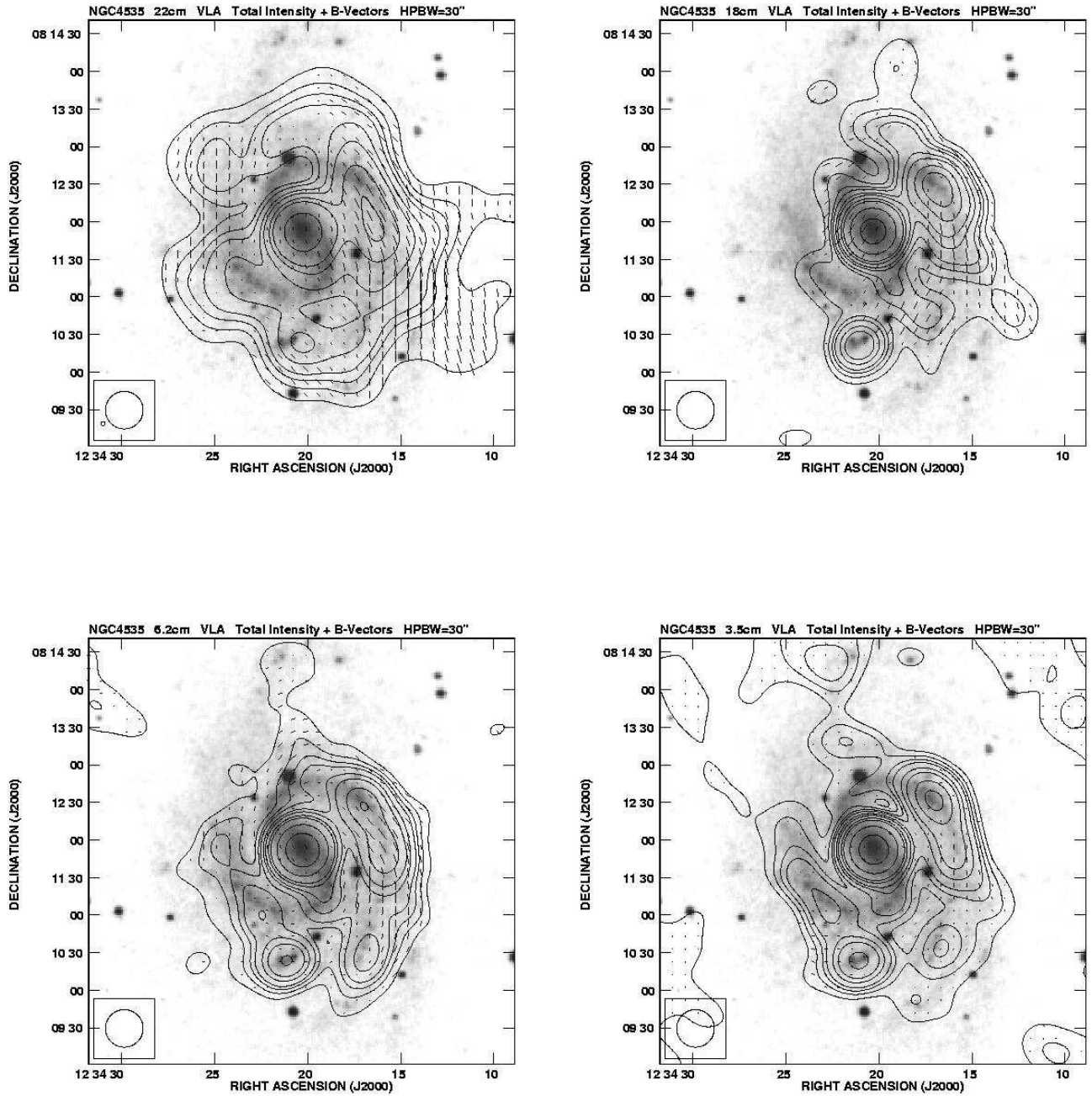


**Fig. 12.** Total intensity contours and the observed  $B$ -vectors of polarized emission of NGC 4535, overlaid onto an optical image from the Digitized Sky Surveys. The contours are as in Fig. 6. A vector of  $1''$  length corresponds to a polarized intensity of  $20 \mu\text{Jy}/\text{beam area}$ .

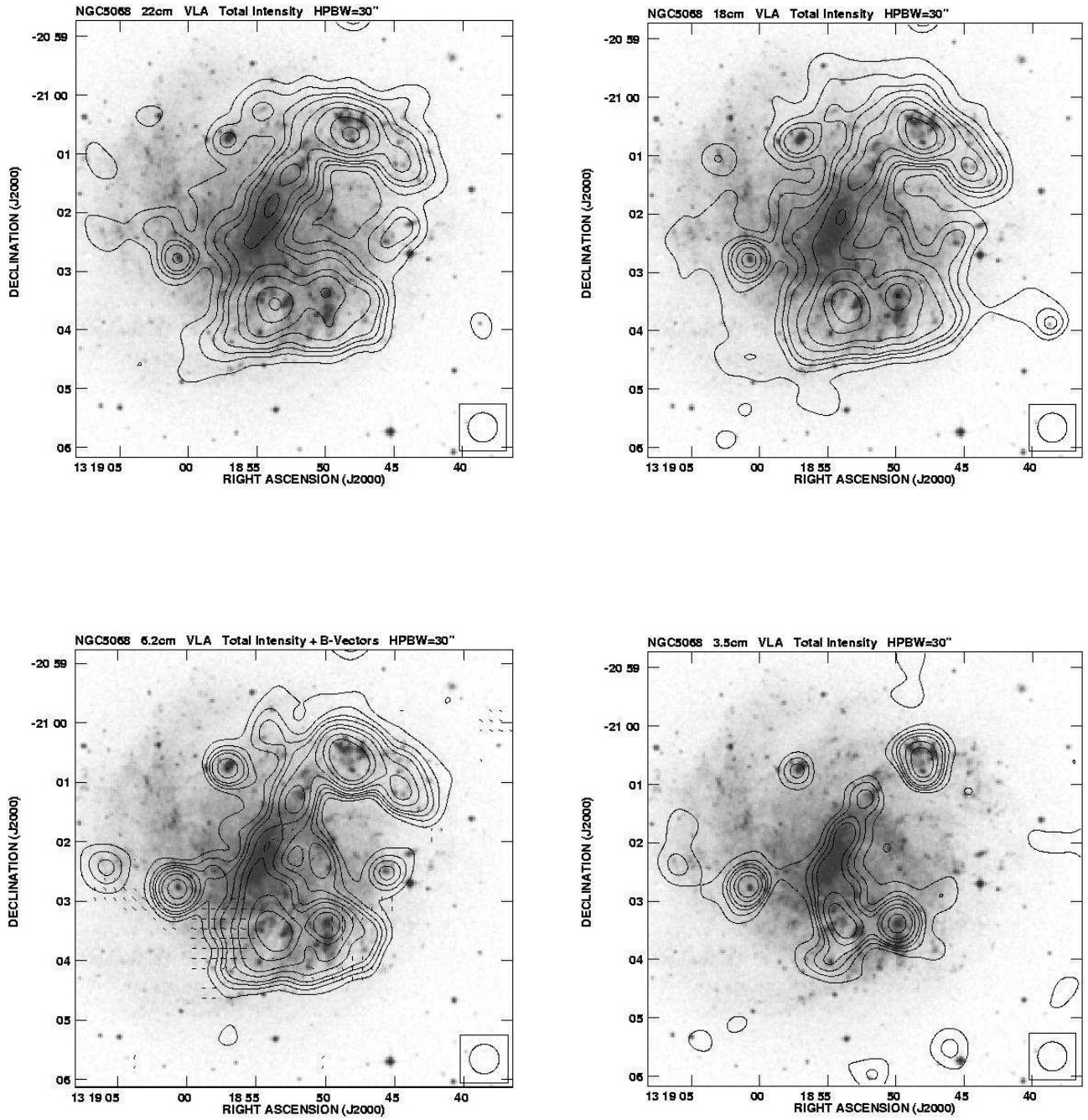


**Fig. 13.** Total intensity contours and the observed  $B$ -vectors of polarized emission of NGC 5068, overlaid onto an optical image from the Digitized Sky Surveys. The contours and the vector scale are as in Fig. 6.

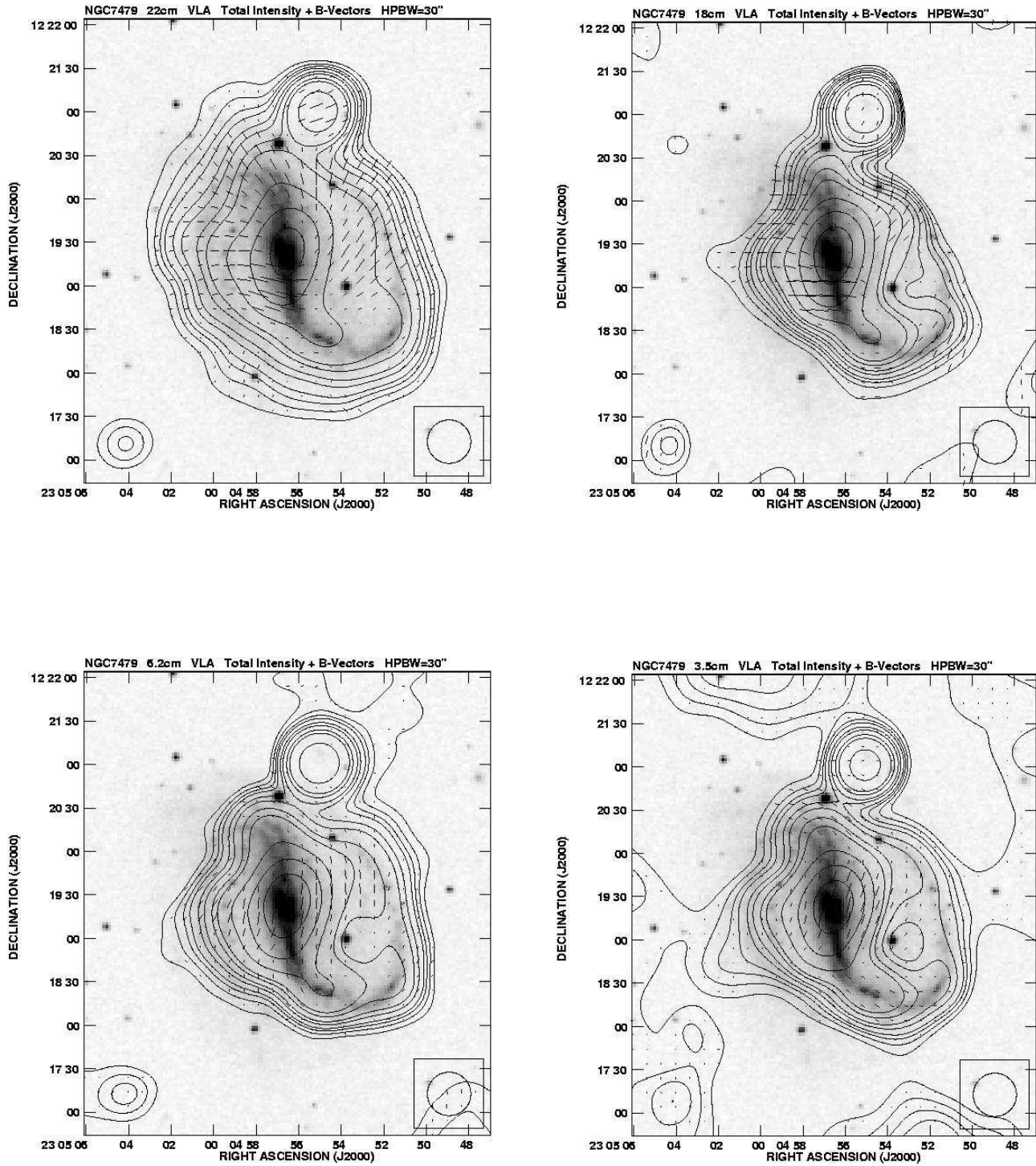


**Fig. 14.** Total intensity contours and the observed  $B$ -vectors of polarized emission of NGC 7479, overlaid onto an optical image from the Digitized Sky Surveys. The contours are as in Fig. 6. A vector of  $1''$  length corresponds to a polarized intensity of  $20 \mu\text{Jy}/\text{beam area}$ .

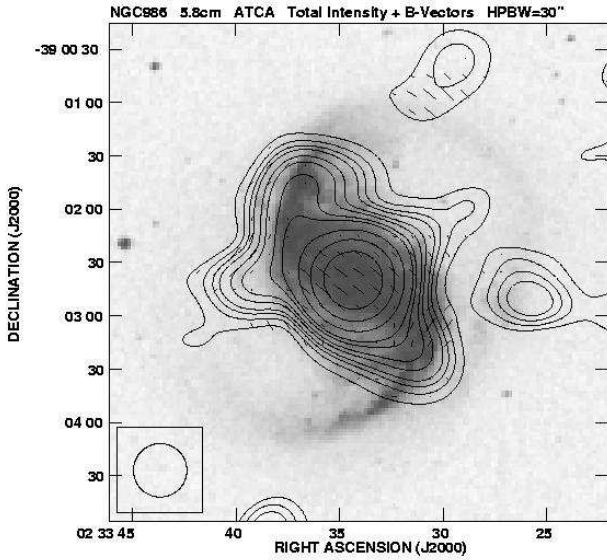


**Fig. 15.** Total intensity contours and the observed  $B$ -vectors of polarized emission of NGC 986, overlaid onto an optical image from the Digitized Sky Surveys. The contour levels are 1, 2, 3, 4, 6, 8, 12, 16, 32, 64, 128  $\times$  the basic contour level of  $100 \mu\text{Jy}/\text{beam}$ . A vector of  $1''$  length corresponds to a polarized intensity of  $10 \mu\text{Jy}/\text{beam}$  area.

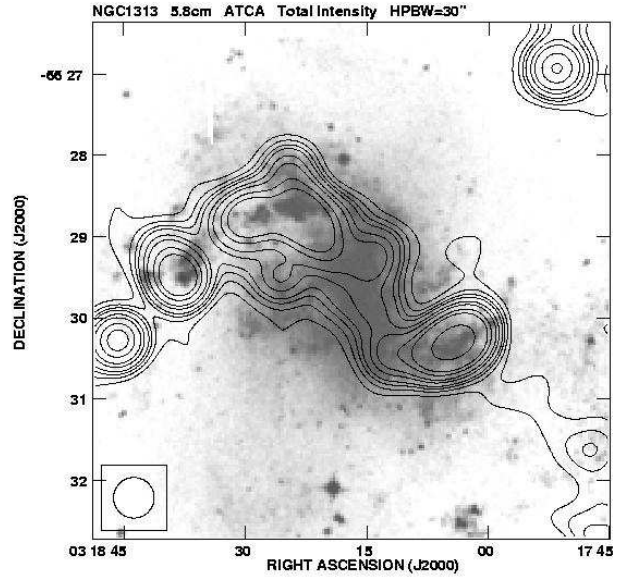


**Fig. 16.** Total intensity contours of NGC 1313, overlaid onto an optical image from the Digitized Sky Surveys. The contours are as in Fig. 15.

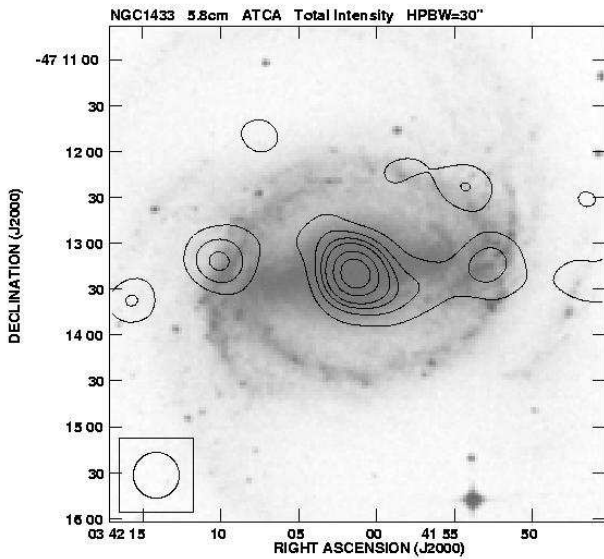


**Fig. 17.** Total intensity contours of NGC 1433, overlaid onto an optical image from the Digitized Sky Surveys. The contours are as in Fig. 15.

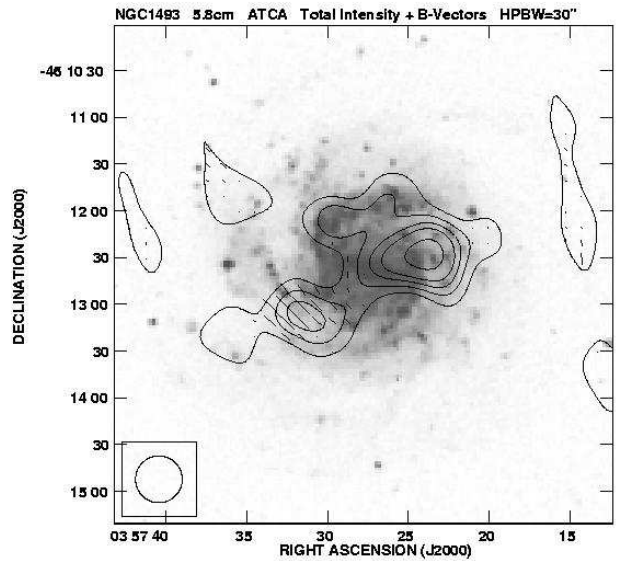


**Fig. 18.** Total intensity contours and the observed  $B$ -vectors of polarized emission of NGC 1493, overlaid onto an optical image from the Digitized Sky Surveys. The contours and the vector scale are as in Fig. 15.



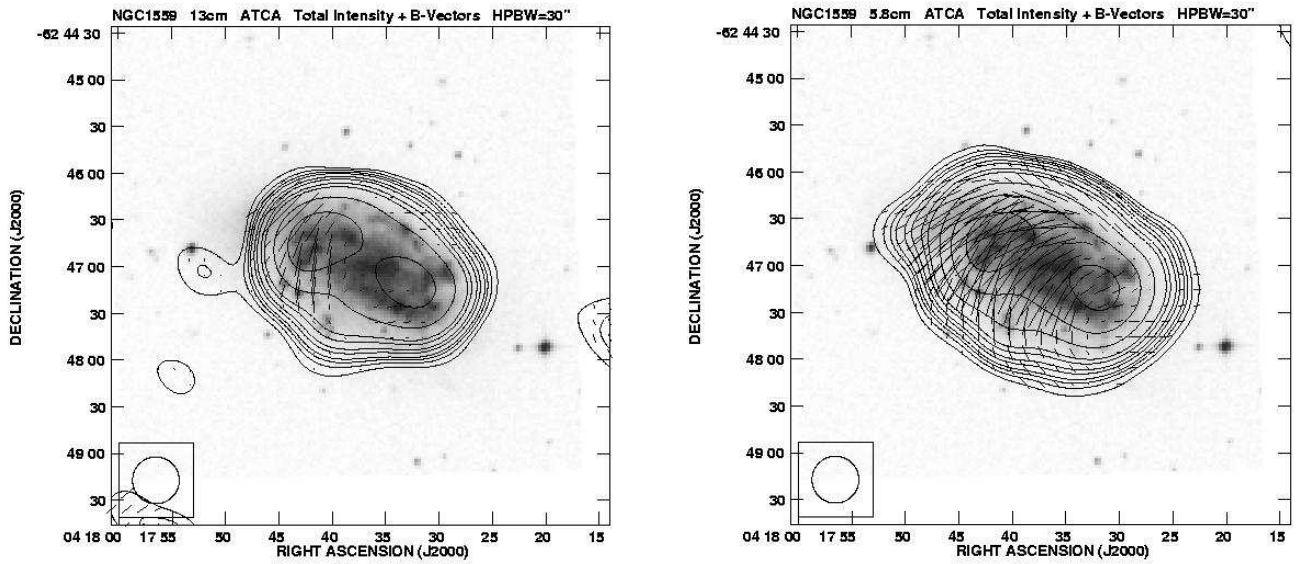


**Fig. 19.** Total intensity contours and the observed  $B$ -vectors of polarized emission of NGC 1559, overlaid onto an optical image from the Digitized Sky Surveys. The basic contour levels are 300 and 100  $\mu\text{Jy}/\text{beam}$ , the contour intervals and the vector scale are as in Fig. 15.

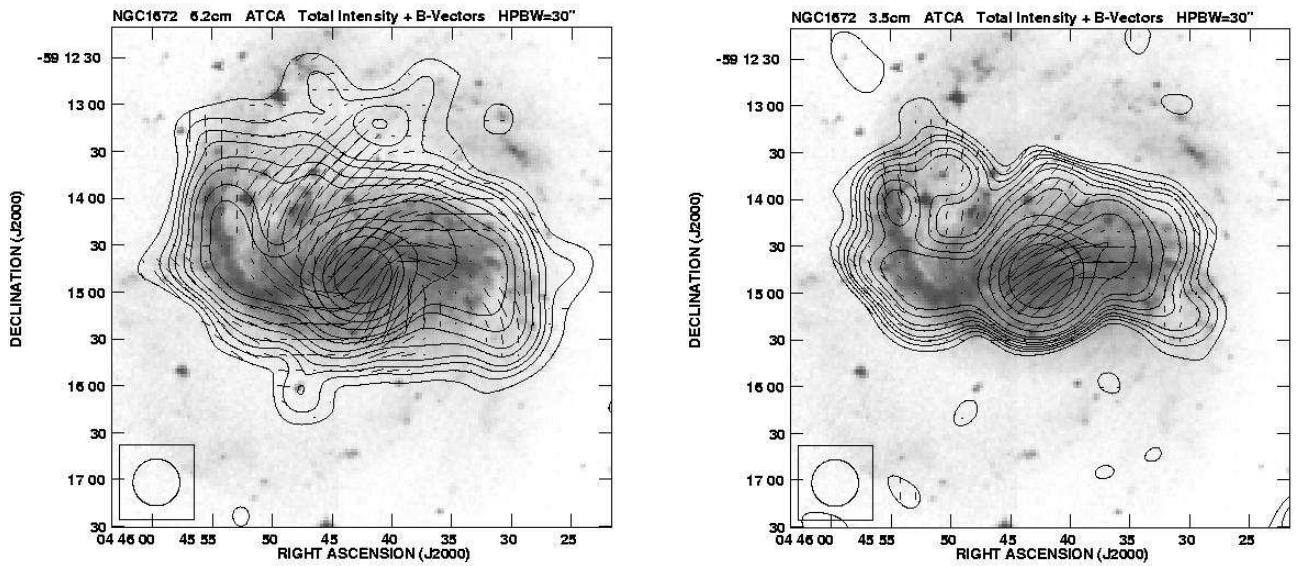


**Fig. 20.** Total intensity contours and the observed  $B$ -vectors of polarized emission of NGC 1672, overlaid onto an optical image from the Digitized Sky Surveys. The basic contour levels are 100 and 40  $\mu\text{Jy}/\text{beam}$ , the contour intervals and the vector scale are as in Fig. 15.

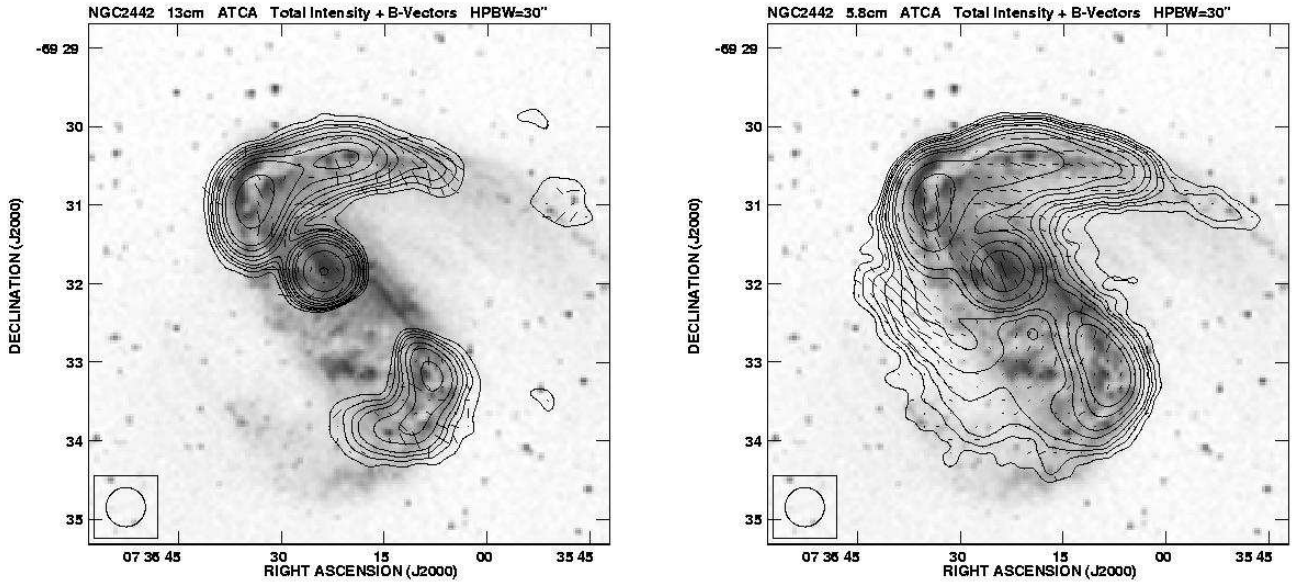


**Fig. 21.** Total intensity contours and the observed  $B$ -vectors of polarized emission of NGC 2442, overlaid onto an optical image from the Digitized Sky Surveys. The contours and the vector scale are as in Fig. 19.

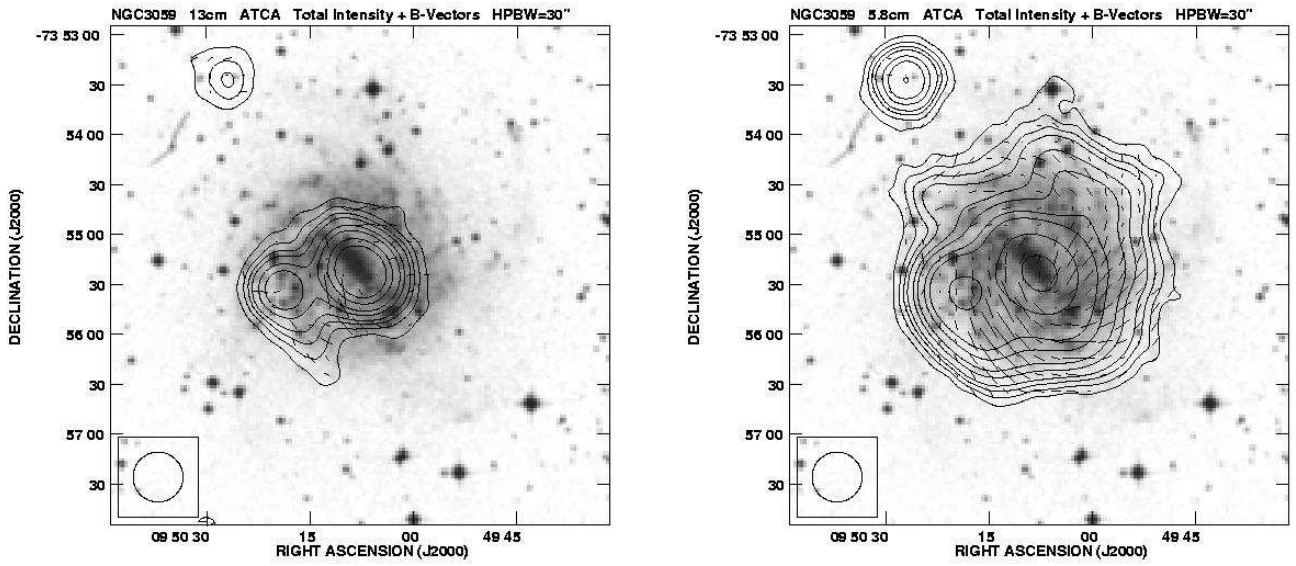


**Fig. 22.** Total intensity contours and the observed  $B$ -vectors of polarized emission of NGC 3059, overlaid onto an optical image from the Digitized Sky Surveys. The contours and the vector scale are as in Fig. 19.

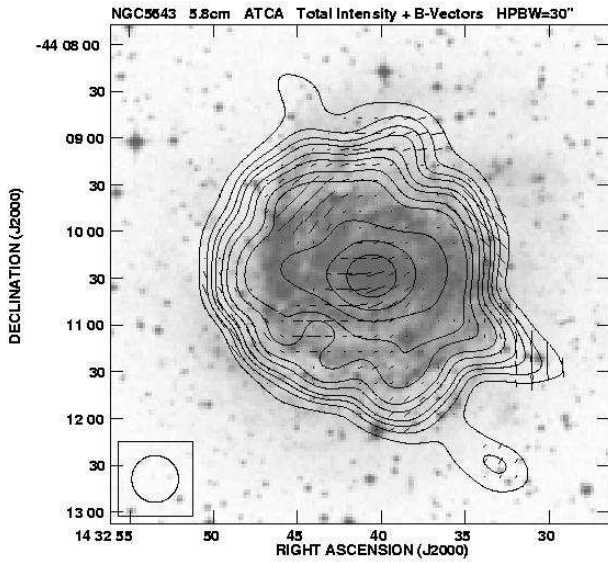


**Fig. 23.** Total intensity contours and the observed  $B$ -vectors of polarized emission of NGC 5643, overlaid onto an optical image from the Digitized Sky Surveys. The contours and the vector scale are as in Fig. 15.

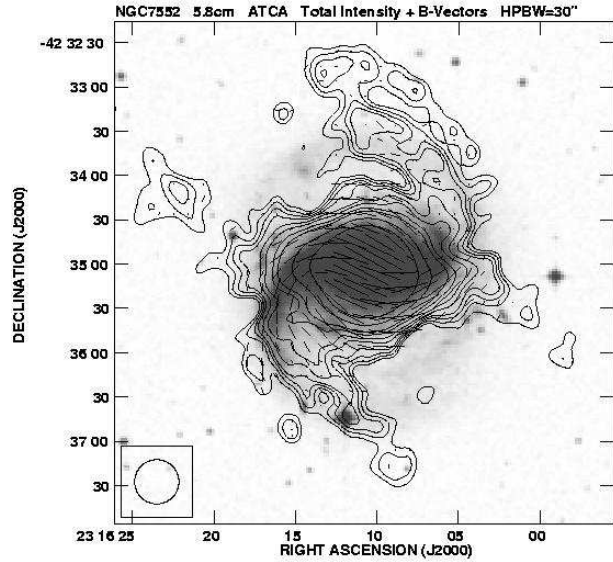


**Fig. 24.** Total intensity contours and the observed  $B$ -vectors of polarized emission of NGC 7552, overlaid onto an optical image from the Digitized Sky Surveys. The contours and the vector scale are as in Fig. 15.

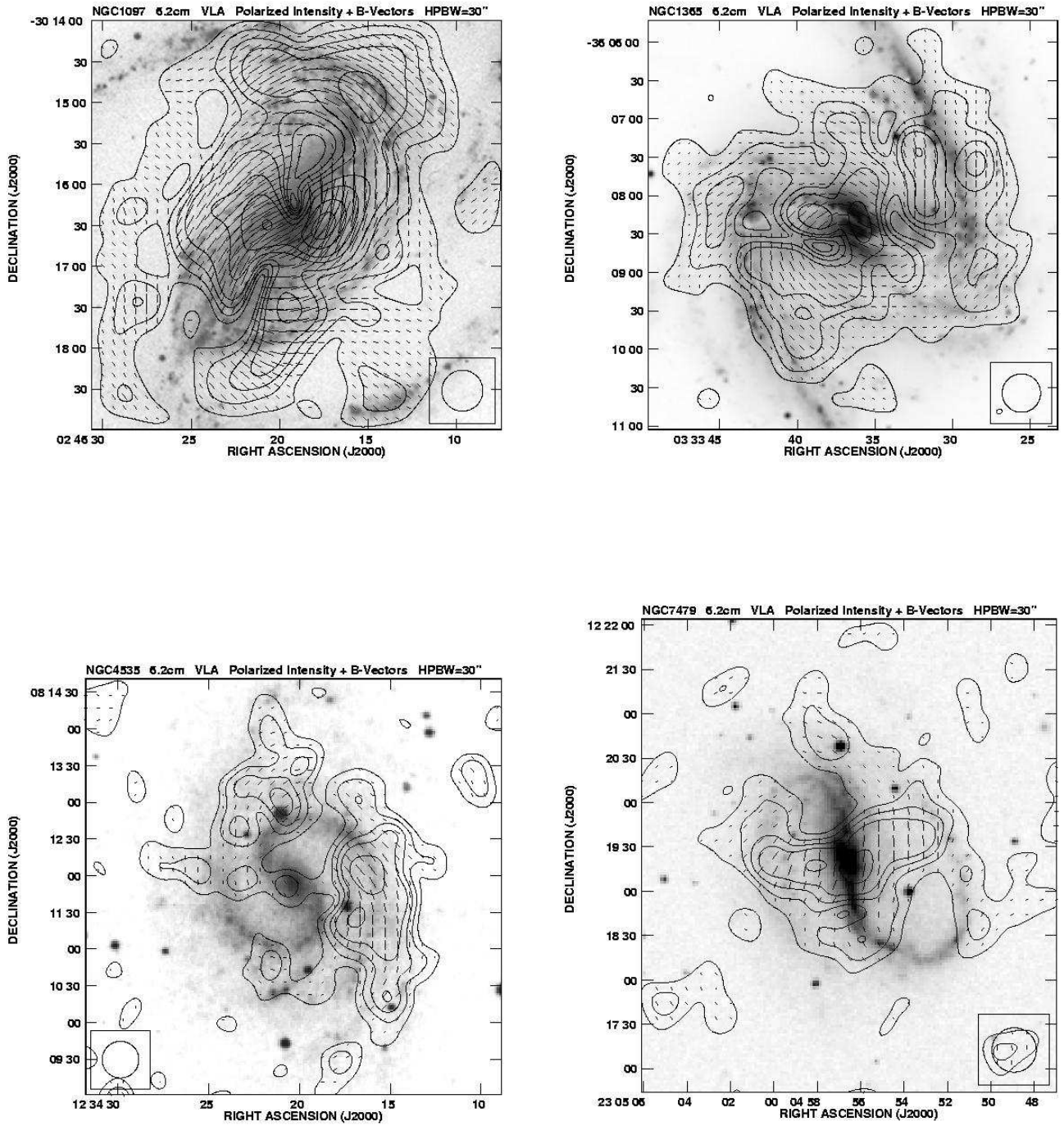


**Fig. 25.** Polarized intensity contours and the observed  $B$ -vectors of NGC 1097, NGC 1365, NGC 4535 and NGC 7479. The contour intervals are 1, 2, 3, 4, 6, 8, 12, 16  $\times$  the basic contour level, which is 50, 30, 30 and 30  $\mu\text{Jy}/\text{beam}$  in the order of increasing NGC number. A vector of  $1''$  length corresponds to a polarized intensity of 20  $\mu\text{Jy}/\text{beam}$  area.

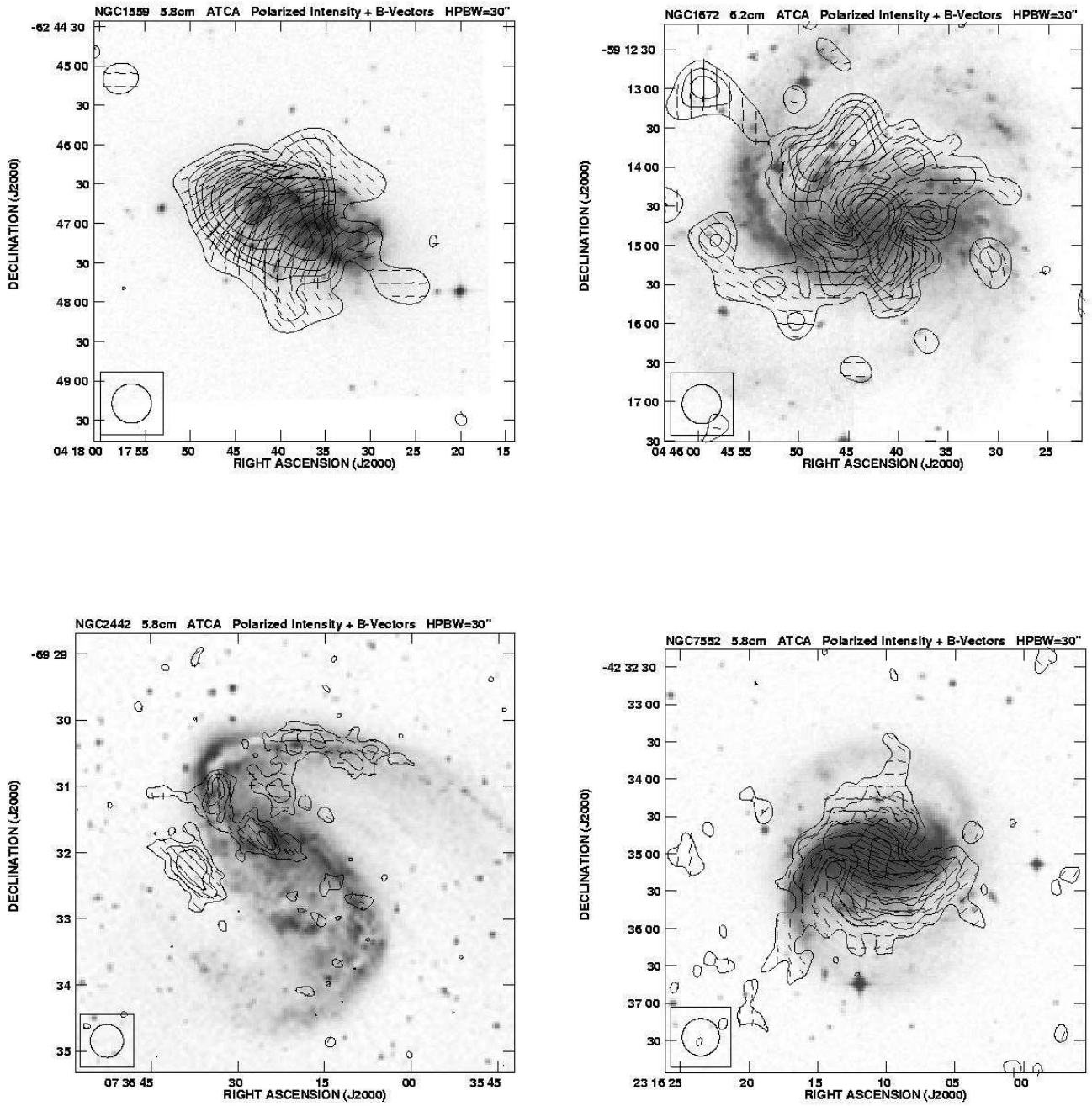


**Fig. 26.** Polarized intensity contours and the observed  $B$ -vectors of NGC 1559, NGC 1672, NGC 2442 and NGC 7552. The contour intervals are 1, 2, 3, 4, 6, 8, 12  $\times$  the basic contour level, which is  $50 \mu\text{Jy}/\text{beam}$ . A vector of  $1''$  length corresponds to a polarized intensity of  $10 \mu\text{Jy}/\text{beam}$  area.